

Article

Energizing Emergency Exit Signs with Wireless Energy Transfer

Mohamed Z. Chaari ^{1,*}, Gilroy P. Pereira ¹, Mohamed Abdelfatah ¹, Rashid Al-Rahimi ¹ and Otman Aghzout ²

¹ FAB-LAB, Qatar Scientific Club, Doha 9769, Qatar; g.pereira@qsc.org.qa (G.P.P.); mohamed.abdelfatah@qsc.org.qa (M.A.); ralrahimi@qsc.org.qa (R.A.-R.)

² SIGL Laboratory, Department of Computer Science Engineering, ENSA, University Abdelmalek Essaadi, Tetouan 93153, Morocco; otmanaghzout@uae.ac.ma

* Correspondence: chaari_zied@ieee.org

Abstract: Emergency exit lights in public buildings are necessary for safety and evacuation. International safety standards require such lighting in many public places, like airports, schools, malls, hospitals, and other spaces, to prevent human casualties in emergencies. Emergency exit lights have become an essential part of casualty reduction projects. They can pose several application problems, including fire safety concerns. The issue of providing a safe way and operating emergency exit lights along one side of a long path arises during an emergency. Many studies in this field consider the case in which emergency exit lights' battery or main power fails. Power failures in dangerous situations such as fires or terrorist attacks make it difficult for people to escape. The lighting in open areas and stairwells during an emergency should be at least 2 lux. This work proposes an innovative technique for wirelessly powering emergency lights using microwave energy. Specifically, the study designed and fabricated a new wirelessly powered emergency lighting prototype. This prototype's wireless power transfer (WPT) base comprises an RF/DC converter circuit and an RF microwave transmitter station. The device can harvest RF microwave energy to energize the emergency light. This research aimed to develop a compact device that captures maximum RF strength to power emergency lights. As a prototype, the proposed device was designed to provide sufficient microwave energy to power an emergency light at 3 W over a 62 m distance.



Citation: Chaari, M.Z.; Pereira, G.P.; Abdelfatah, M.; Al-Rahimi, R.; Aghzout, O. Energizing Emergency Exit Signs with Wireless Energy Transfer. *energies* **2023**, *16*, 5080. <https://doi.org/10.3390/en16135080>

Academic Editors: Enrique Romero-Cadaval and Byoung Kuk Lee

Received: 29 May 2023

Revised: 21 June 2023

Accepted: 26 June 2023

Published: 30 June 2023



Copyright: © 2023 by the authors. Licensee MDPI, Basel, Switzerland. This article is an open access article distributed under the terms and conditions of the Creative Commons Attribution (CC BY) license (<https://creativecommons.org/licenses/by/4.0/>).

1. Introduction

A building's emergency lighting is designed to provide sufficient illumination on the exit path. An emergency exit light provides its average illumination level when the power supply is active and works on battery energy at a low illumination level when there is a primary power supply outage. This device permits the occupants to safely exit the building in case of a mains power failure or emergency. In a fire, this feature can save many lives. When a fire spreads in a building, people become terrified. As a result, households and residents must follow fire safety protocols. Darkness only makes people feel disoriented and increases their chances of getting injured or dying in such situations. Consequently, buildings should have well-lit exit signs to reduce injuries and death. People can evacuate buildings more easily with adequate exit signage when fires break out.

Under the Australian Building Code, emergency lighting must be provided for all types of construction, except for non-habitable structures and single standalone residences [1]. Additionally, according to National Fire Protection Association (NFPA) Life Safety Code 101, all commercial buildings must have emergency and exit path lighting [2]. The construction product directive specifies that prompt lighting in a specific area should be provided automatically and appropriately when the regular power supply is lost. Lighting must conform to BS 5266-1 and BS EN 50172 [3]. Compared with other high-income countries, the US experiences more long-lasting power failures. US citizens experience over

seven hours of power interruptions each year [4], compared with only twenty-one minutes in Japan each year [5]. It may be challenging for occupants to navigate a building safely during a power outage. Navigating areas such as offices, warehouse areas, staircases, washrooms, and other spaces with little or no natural illumination can be difficult, especially when emergency lighting is unavailable or not working.

Typically, emergency signs have a battery life of three to five years [6]. Many issues can cause a battery to fail during this period, such as excessive temperatures, storing emergency lighting for an extended period before mounting it, and keeping emergency batteries discharged for a long time [7]. Building occupants and guests are left in the dark if these safety devices do not function when needed.

Many people die because of the failure of emergency lighting worldwide. On 9 June 2018, the death of an 80-year-old man at Aberdeen Market could have been prevented, had the company running the site installed and maintained adequate emergency lighting [8]. Market Village Company Ltd., L34 5GA Prescot, UK, was prosecuted for violating the Fire (Scotland) Act 2005. Such situations call for sufficient-intensity lighting in the event of an emergency.

This research study aimed to manufacture an emergency exit light that can be powered by an alternate source during a power outage if mainline power and backup batteries fail.

Figure 1 shows emergency exit signs placed near the exit door in schools and universities.



Figure 1. Use of emergency lighting in schools and universities [9].

If there is an emergency and the exit route runs through open areas, there should be at least 1 lux of lighting, according to the BS 5266-1 standard [10]. A well-illuminated emergency exit sign must have luminance greater than 2 cd/m^2 or 2 lux for any 10 mm patch area of the sign according to ISO 3864 standards [11]. A luminaire with LEDs producing at least 2 lux requires a power of around 2 W. We developed a wireless system that powers emergency luminaires from a distance of 62 m.

Power transmission without a wire or physical link is known as wireless power transmission. WPT is mainly used where it is not easy to transfer energy using conventional cables. Researchers encounter the same common challenges regarding microwave power transmission, like antenna design, scattering, interference, budget, safety issues, and environmental risks. For microwaves to be efficient, all the RF energy transmitted by the RF source must be incident on the wave collection antenna [12]. When RF energy travels across space, it must diffract because it must pass through an aperture, which, at a shorter wavelength, gives a more focused beam. However, atmospheric disturbances also account for losses in WPT [13]. Microwave transmissions are not generally hindered by significant attenuation loss due to Rayleigh scattering, because the transmitted wavelengths tend to be long enough to mitigate this effect. As a result, proposals for microwave transmission over long distances, in both atmosphere and space, must account for large transmitting and receiving antennas due to the Rayleigh criterion.

Research and development in the field of wireless power transfer (WPT) focus on reviving devices and communicating wirelessly during crises. WPT is suitable for various applications, including powering abandoned sensors, actuators, and microdevices with low power consumption. MD Amanath Ullah and his team provided a well-rounded review of recent advancements in receiving antennas for radio-frequency energy harvesting and

WPT as two emerging alternative energy technologies [14]. Dr. Saeideh Pahlavan and her team explored the use of star-shaped coils for free-moving WPT applications [15]. WPT technology is beneficial in hazardous environments and transportation fields, especially in aeronautics and space. In general, it is used to monitor certain functions on board drones or flying objects.

The US Army recently implemented wireless chargers for devices that can be recharged from fifteen meters away [16]. An announcement by the US Army states that the branches' research and development centers will contribute over USD 6 million towards improving wireless energy transmission efficiency. Chaari et al. developed a study regarding the impact of wireless power charging on the future of the battlefield [17].

Due to recent advances in information technology and electronics, as well as the constant development of wireless communication protocols, the number of portable single-purpose devices connected to the global network has increased dramatically. The above-mentioned devices usually have a relatively simple electronics design and are designed to perform one specific function, such as monitoring, detection, or alarm [18,19]. They are commonly called Internet of Things (IoT) devices. IoT development and implementation pose a few challenges. Power management stands out most prominently [20,21]. Compact IoT devices do not require vast amounts of energy, are usually located in hard-to-reach places, and may be dispersed over long distances, making it uneconomical to power them with wires when combined. There are several ways to power IoT devices without direct connection to the electricity grid [22–24] using different energy sources [25]. The present paper focuses on wireless power transfer using electromagnetic radiation.

The multiband combined RF energy harvester developed by Kuhn is a practical example of a device that relies exclusively on power harvested from ambient electromagnetic fields [26]. The research study evaluates several topologies of RF energy harvesters, considering the need to convert electromagnetic energy into direct current at four different frequencies. The resulting multiband antenna converts RF energy with up to 84% efficiency. Kuhn, however, points out that DC interference among radio-frequency channel branches can affect the results. Muncuk's innovative approach combines signals from multiple input antennas [27]. The author proposes an energy harvester topology based on a four-stage Dickson voltage rectifier and two configurable capacitors as part of a tunable circuit.

According to experimental results, the converter was demonstrated to be capable of achieving an efficiency rate of up to 24%. More conventional designs of impedance-matching circuits provide better performance characteristics. Huang described a dynamic impedance-matching circuit based on a series of capacitors [28]. The research study claimed that it achieved a high and stable conversion efficiency rate of around 75%. A thorough analysis of loss sources is the key to designing a highly efficient wireless power transfer system. Chen stresses the fact that the insertion of a matching element in rectenna circuits leads to a critical decrease in output power due to parasitic losses in capacitors, inductors, and transmission lines [29]. Observed results show that up to 95% of power dissipates at various frequencies due to the use of the components.

It should be noted that to avoid unexpected frequency shifting, the electrical parameters of both rectifying and matching circuits should be considered in the stage of antenna design. Farias proposed a novel rectenna design methodology [30]. The proposed design method divides the system design process into several consecutive steps. Accurate results were achieved by only using one intermediate sample for input power calibration. The calculation results were validated with an experiment and showed a discrepancy rate as low as 13%.

The present paper describes a microwave system and a rectenna designed to harvest maximum microwave energy. The proposed system was fabricated and assembled, and its performance was evaluated.

There are two main subsystems in the prototype design. The first subsystem comprises a magnetron RF transmitter coupled with a pyramidal horn antenna. The second subsystem is the emergency exit sign, which consists of an RF/DC convertor and a patch antenna. The

subsystems are highlighted in Figure 2. A rectenna was placed inside an emergency exit sign made of acrylic, as shown in Figure 3a. Figure 3b,c show the front view and back view of the rectenna, respectively.

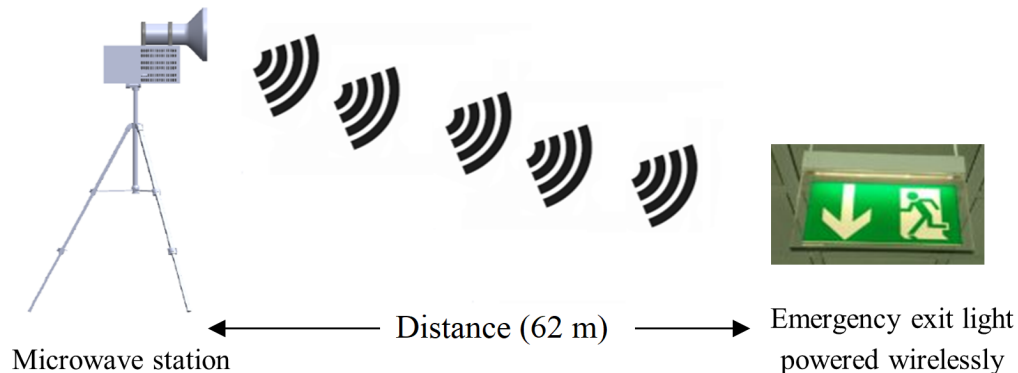
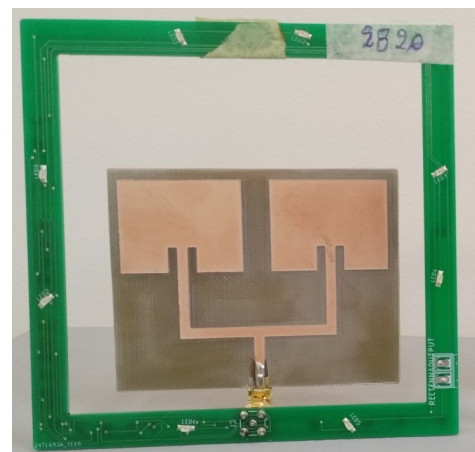


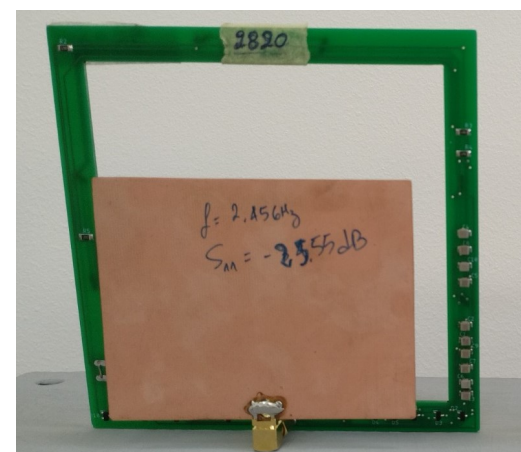
Figure 2. Powering emergency exit lights wirelessly.



(a) Two harvesting circuits inserted inside the emergency sign box.



(b) The front view of the rectenna.



(c) The back view of the rectenna.

Figure 3. The new emergency lighting consists of an RF power harvesting circuit.

The remainder of the paper is organized as follows: The RF microwave transmitter station design and RF power budget are presented in Section 2, followed by the power harvesting

device simulation results and rectifier investigation in Section 3. Results and discussion of the prototype are presented in Section 4. The paper's conclusions are presented in Section 5.

2. RF Microwave Transmitter and Power Budget

2.1. RF Microwave Transmitter Station Design

In this application, 2.45 GHz was chosen because of the increase in antenna size at low frequencies. The operating frequency of 2.45 GHz is suitable for radio signals and microwave ovens, and 2.45 GHz WPT technology is also efficient. These bands are already allocated to several radio services under the ITU-R radio regulation. Furthermore, they can be used for industrial science and medicine (ISM applications). Currently, ISM is considered a local band. High-energy waves, optical rays, and radio waves are all types of electromagnetic radiation. We used low-priced, commercially available microwave magnetron tubes as sources for the 2.45 GHz transmitter. The microwave generator utilized in this experiment was a magnetron with operating frequency of 2450 MHz and RF power of 500 W.

There were two power systems in the magnetron power supply circuit, one at low voltage (3.2 V) and one at high voltage (4.5 kV), as shown in Figure 4 [31].

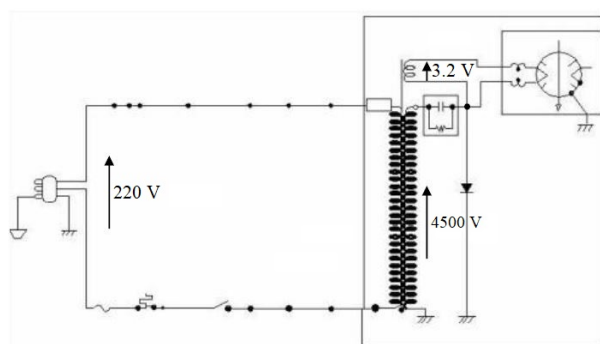


Figure 4. The electrical circuit of the magnetron.

As illustrated in Figure 5, these RF transmitter systems comprised a waveguide launcher, a magnetron, an HV transformer, electrical supply, and a pyramidal horn antenna in a compact enclosure. They are characterized by high gain and directivity and are easy to manufacture locally.

In this prototype, we utilized a horn antenna, which can be widely applied to electromagnetic waves with wavelengths between centimeters and millimeters [32]. The radiation pattern produced by antennas with horns can range between 100° and 140°, while that produced by antennas with pyramidal horns can range between 10° and 20°. Increasing the geometric dimension of the horn prevents the further narrowing of its directivity pattern [33]. A wide spectrum of operating frequencies, high directivity, large limiting power of the microwave signal, and ease of manufacturing are the main advantages of this antenna. Before fabricating a prototype, CST software was utilized to simulate optimal horn antenna specifications, as shown in Figure 6. For the modeled RF horn antenna, the signal was excited through the magnetron antenna. Simulation-optimized designs were obtained using time-domain analysis tools in CST, which provide a wide range of time-domain signals. We optimized the horn antenna parameters according to magnetron specifications, pin height, pin diameter, and the antenna metal wall thickness. We used these characteristics to evaluate the proposed design.

We used CST microwave simulators to simulate and optimize the RF transmitting antenna. The main focus was microwave radiation, S-parameters, gain, voltage standing wave ratio (VSWR), and power transmission. Their radiation patterns determine the maximum gain, directivity, and functional area of pyramidal horn antennas. Figure 7a,b show a sketch of a pyramidal horn antenna.



Figure 5. The microwave transmitter (0.5 kW).

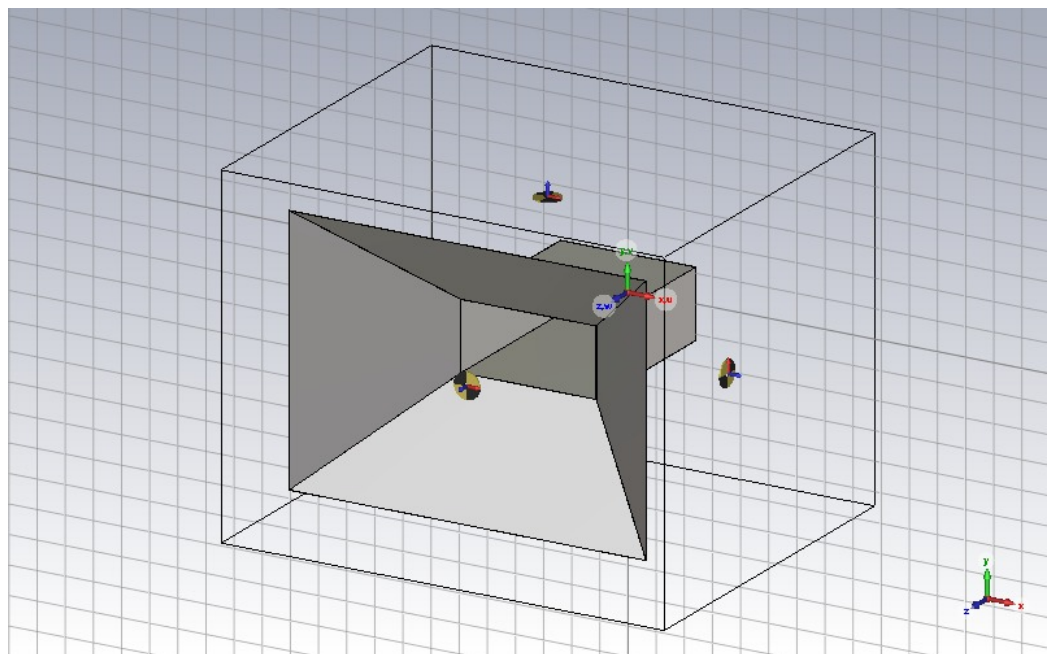


Figure 6. The horn antenna structure developed with CST.

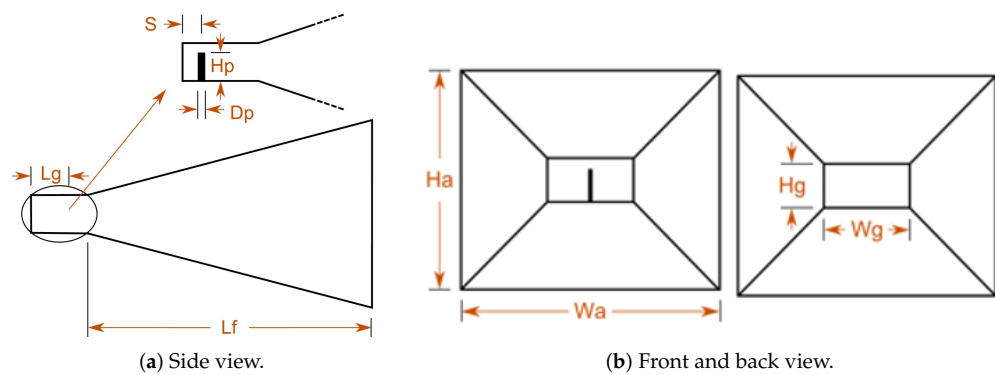


Figure 7. Pyramidal horn antenna sketches.

The gain of a horn antenna is [34]

$$G = \frac{4\pi}{\lambda^2 \epsilon_{ap} W_g H_g} \quad (1)$$

The waveguide dimensions were

$$W_g = 0.8382 \times \lambda = 96.05 \text{ mm (Waveguide width)} \quad (2)$$

$$H_g = 0.3925 \times \lambda = 48.02 \text{ mm (Waveguide length)} \quad (3)$$

The aperture dimensions were as follows:

$$\begin{aligned} W_a &= 253.64 \text{ mm (Aperture width)} \\ H_a &= 183.18 \text{ mm (Aperture height)} \end{aligned}$$

The flare length was

$$L_f = 76.78 \text{ mm}$$

The metal wall thickness of the horn antenna was

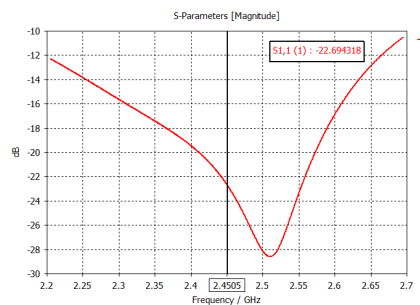
$$T_s = 0.001 \times (\lambda) = 0.001 \times 124.913 = 0.1249 \text{ mm} \quad (4)$$

Table 1 presents parameters regarding the horn antenna, including waveguide length, waveguide width, flare length, aperture height, aperture width, antenna wall thickness, and other parameters. Initially, the pyramidal horn antenna had dimensions of $W_a = 253.64$ mm aperture width, $H_a = 183.18$ mm aperture height, 76.78 mm flare length, $W_g = 96.05$ mm waveguide width, and $H_g = 48.02$ mm waveguide height. We discuss and analyze the results in the following sections.

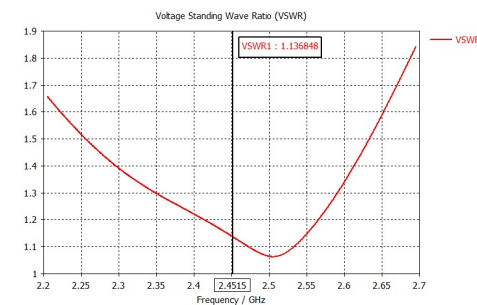
An antenna's reflection coefficient is one of the most important factors to consider when determining its power output. An excellent antenna requires a return loss value of less than -10 dB. Figure 8a demonstrates an ideal return loss of -22.69 dB at 2.45 GHz. The VSWR value is recommended to fall between 1 and 2 for the best communication [35]. If the impedance-matching value is close to 1, it is optimal. The VSWR of the horn antenna was 1.13, and the frequency range was 2.4119 GHz to 2.4913 GHz, as shown in Figure 8b. A Smith chart highlighting S_{11} is illustrated in Figure 8c. The antenna bandwidth was approximately 433 MHz (19.34%). Based on the 3D radiation pattern graphs, we concluded that the antenna had a maximum gain of approximately 12.77 dBi and was very directive, as shown in Figure 8d,e, correspondingly.

Table 1. List of pyramidal horn antenna parameters.

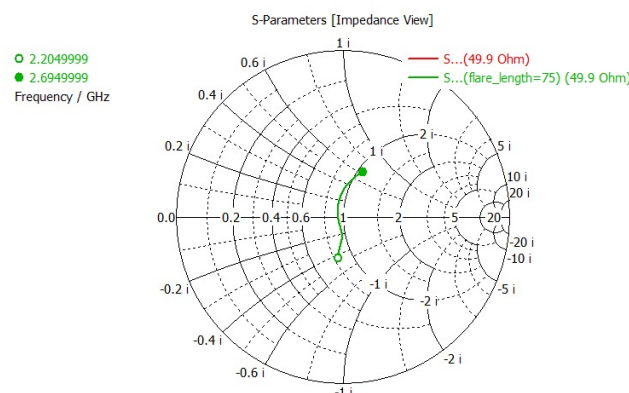
Name	Value	Description
wavelength_centre	122.364 mm	
waveguide_width	96.055 mm	Waveguide width
waveguide_length	122.364 mm	Waveguide length
waveguide_height	48.027 mm	Waveguide height
pin_inset	22.989 mm	Feed pin inset (distance from the back wall)
pin_height	27.661 mm	Feed pin height
pin_diameter	1.223 mm	
metal_thickness	0.124 mm	Antenna metal thickness
frequency_centre	2.45 GHz	Centre frequency
flare_length	76.78 mm	Flare length
S	299.792458 m/s	Speed of light (corrected for the model units)
aperture_width	253.645 mm	Aperture width
aperture_height	183.183 mm	Aperture height



(a) Return loss vs. frequency of the antenna.



(b) VSWR.



(c) Smith chart.

Figure 8. Cont.

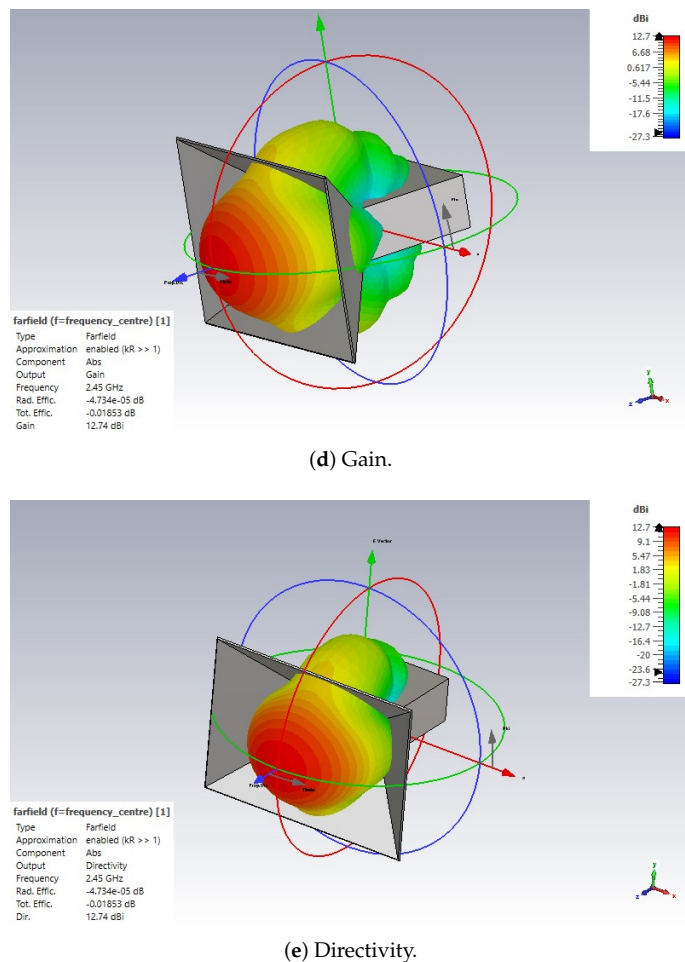


Figure 8. Simulation of the horn antennas.

The phase errors on the H-plane were

$$t = \frac{W_a^2}{8\lambda L_1} = 0.1276 \quad (5)$$

The phase errors on the E-plane were

$$s = \frac{H_a^2}{8\lambda L_2} = 0.0714 \quad (6)$$

The phase error (t) on the H-plane differs from the phase error (s) on the E-plane.

The electric field components are generated by the antenna and carried into space by the waveguide. The magnetron feed pin is placed at the center of the " H_a " wall, parallel to the " H_b " wall, and at a one-quarter wavelength distance from the short end of the waveguide, as shown in Figure 9. There is a maximum E field in a dominant mode, so there is also an optimal energy transfer (coupling).

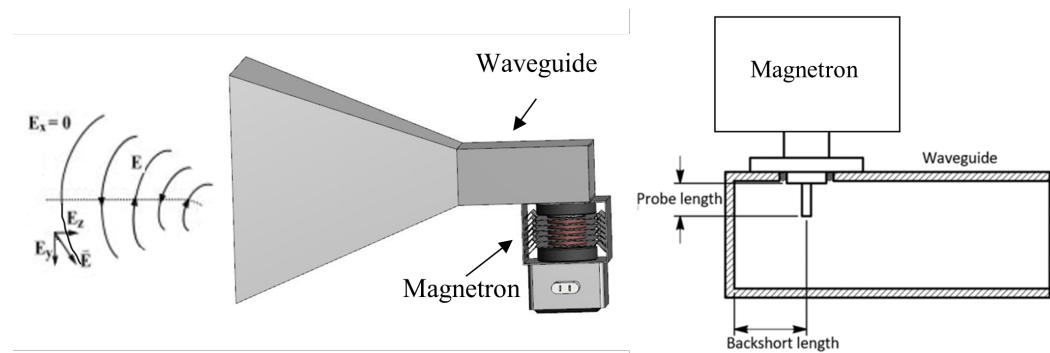


Figure 9. RF magnetron placement on the horn antenna.

In the above, the following apply:

Back short length = 26 mm;

Probe length = 16.36 mm.

The above simulation had to be modified by changing two parameters according to the magnetron feed pin height and pin diameter. We also adjusted the thickness of the metal antenna to 2 mm.

The magnetic antenna feed pin measured 26 mm in height and 16.36 mm in diameter, as shown in Figure 10a,b, respectively. For an optimal simulation, we modified the three parameters in the CST microwave: the feed pin height, the feed pin diameter, and the antenna metal thickness. Table 2 presents the optimal parameter values of the horn antenna, such as waveguide width, waveguide length, aperture width, and aperture length, where the modified parameters are highlighted in red.



(a) Feed pin height measurement.

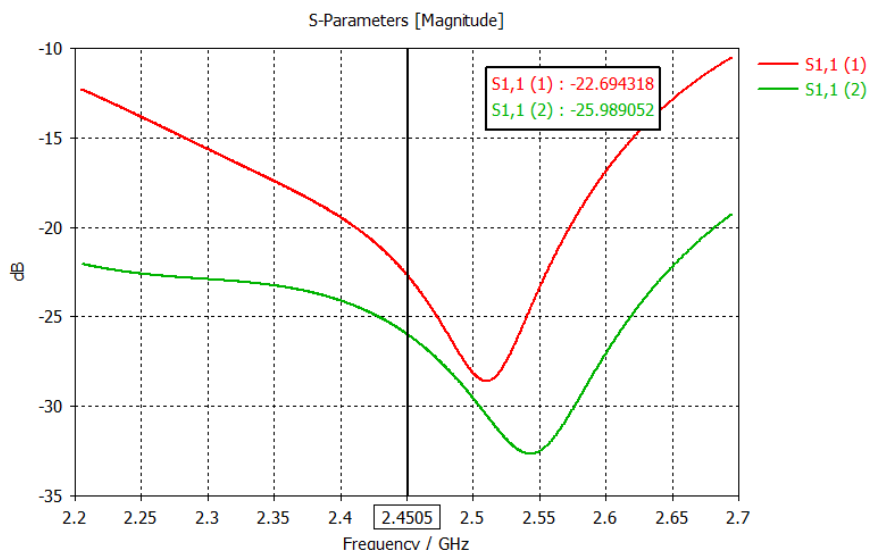
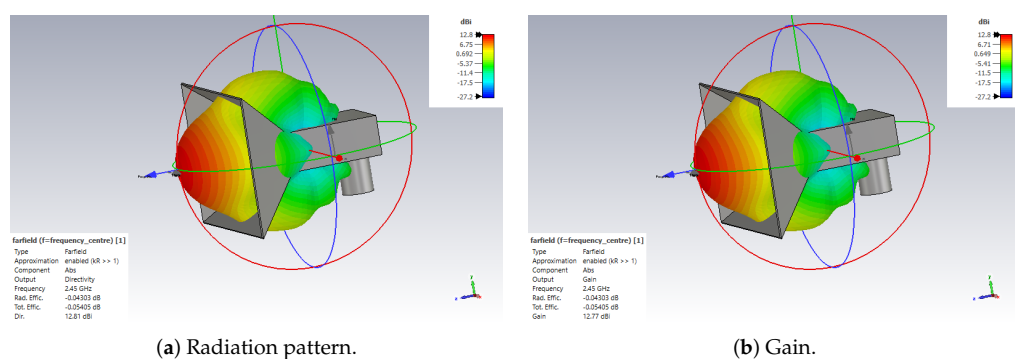
(b) Feed pin diameter measurement.

Figure 10. Measurement of magnetron antenna (feed pin).

Figure 11 demonstrates the ideal return loss of -25.98 dB at 2.45 GHz . We concluded from the 3D radiation pattern plots shown in Figure 12a,b that the antenna was very directive, with a maximum gain of approximately 12.8 dBi . The horn antenna bandwidth was approximately 433 MHz (19.34%), and the VSWR was 1.10, as illustrated in Figure 13.

Table 2. Optimal antenna parameters.

Name	Value	Description
wavelength_centre	122.364 mm	
waveguide_width	96.055 mm	Waveguide width
waveguide_length	122.364 mm	Waveguide length
waveguide_height	48.027 mm	Waveguide height
pin_inset	22.989 mm	Feed pin inset (distance from the back wall)
pin_height	26	Feed pin height
pin_diameter	16.36	Feed pin diameter
metal_thickness	2	Antenna metal thickness
frequency_centre	2.45 GHz	Centre frequency
flare_length	76.78 mm	Flare length
S	299.792458 m/s	Speed of light (corrected for the model units)
aperture_width	253.645 mm	Aperture width
aperture_height	183.183 mm	Aperture height

**Figure 11.** An optimal horn antenna's reflection coefficient.**Figure 12.** Three-dimensional far-field radiation pattern simulation results of the optimal horn antenna.

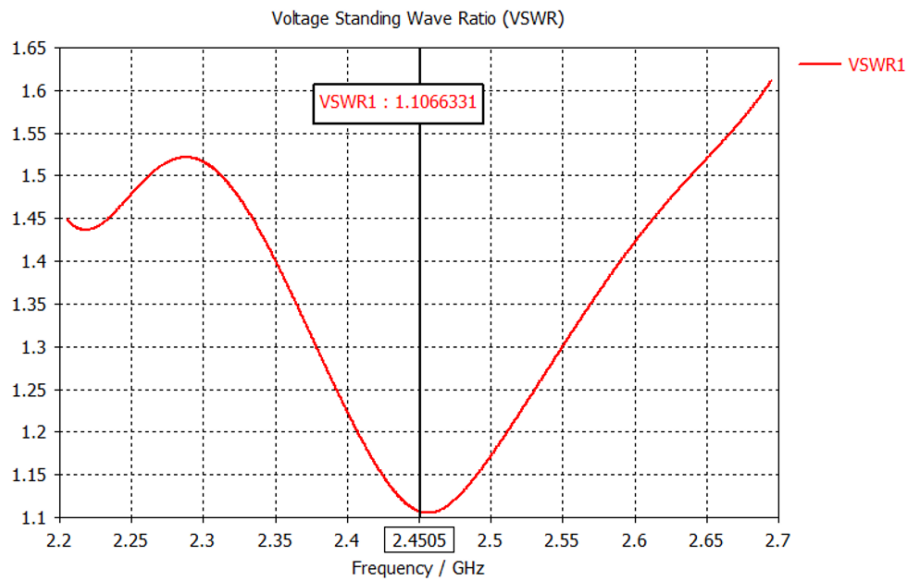


Figure 13. Frequency vs. VSWR based on simulations.

Figure 14a highlights flare length L_f and slant height ρ_e on the e-plane, while Figure 14b highlights flare length p_h and slant height ρ_h on the h-plane. The gain of the pyramidal horn antenna is shown in Equation (7) [36]:

$$G = \frac{4\pi}{2\lambda^2} W_a H_a \quad (7)$$

We can calculate the aperture height using Equation (8) and the aperture width with Equation (9):

$$H_a = \sqrt{2\lambda\rho_e} \quad (8)$$

$$W_a = \sqrt{3\lambda\rho_h} \quad (9)$$

The flare length on the E-plane and H-plane can be calculated as

$$L_f = (H_a - H_g)[(\frac{\rho_e}{H_a})^2 - \frac{1}{4}]^{\frac{1}{2}} \quad (10)$$

$$p_h = (W_a - W_g)[(\frac{\rho_h}{W_a})^2 - \frac{1}{4}]^{\frac{1}{2}} \quad (11)$$

Equations (10) and (11) show that the flare lengths on both planes are directly proportional to the slant heights. The slant heights, in turn, are proportional to the aperture widths and heights, as seen in Equations (8) and (9). Hence, increasing the flare length of the RF transmitting antenna increases its gain.

The directivity of a pyramidal horn antenna is given by

$$D = \frac{4\pi}{\lambda^2} \epsilon_t \epsilon_{ph}^E \epsilon_{ph}^H AB \quad (12)$$

Using the data in Table 2, we designed an optimum horn to provide low return loss at 2.45 GHz. We changed the flare length to 207 mm from 76.78 mm and kept the aperture dimensions of $W_a = 253.64$ mm and $H_a = 183.18$ mm. As seen in Figure 15a,b, the gain of the proposed design increased to 14.64 dBi at 2.45 GHz, and S_{11} was equal to -23.38 dB, respectively.

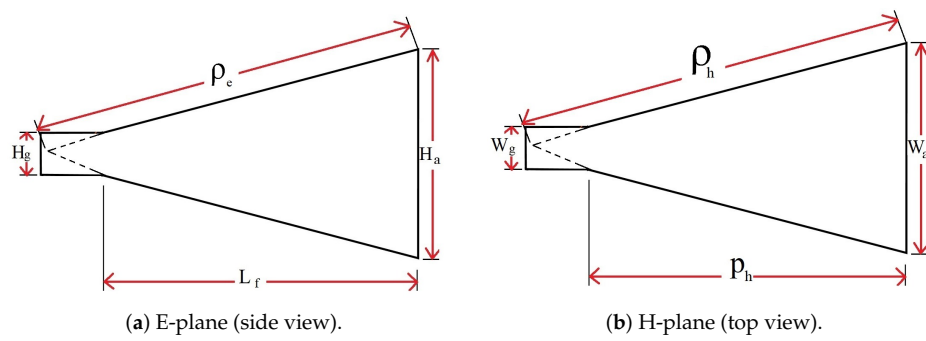
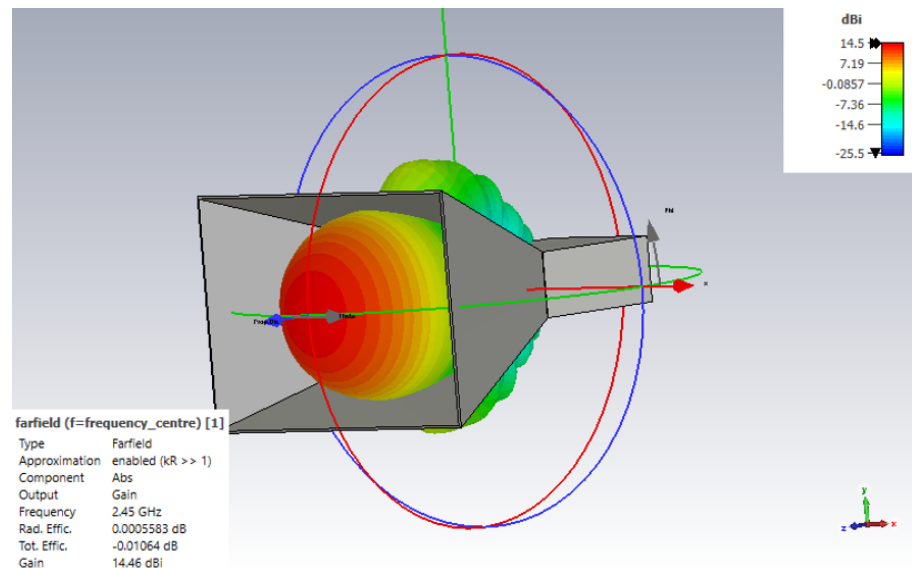
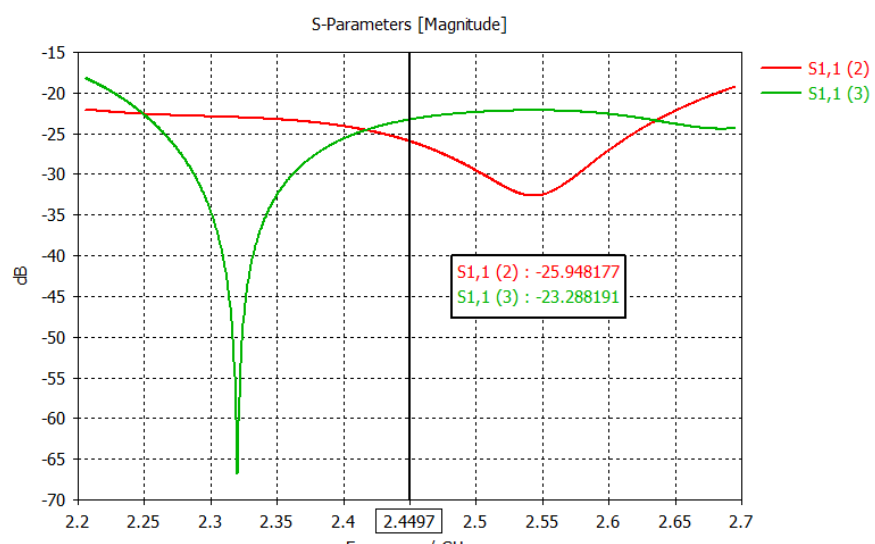


Figure 14. Pyramidal horn antenna parameters.



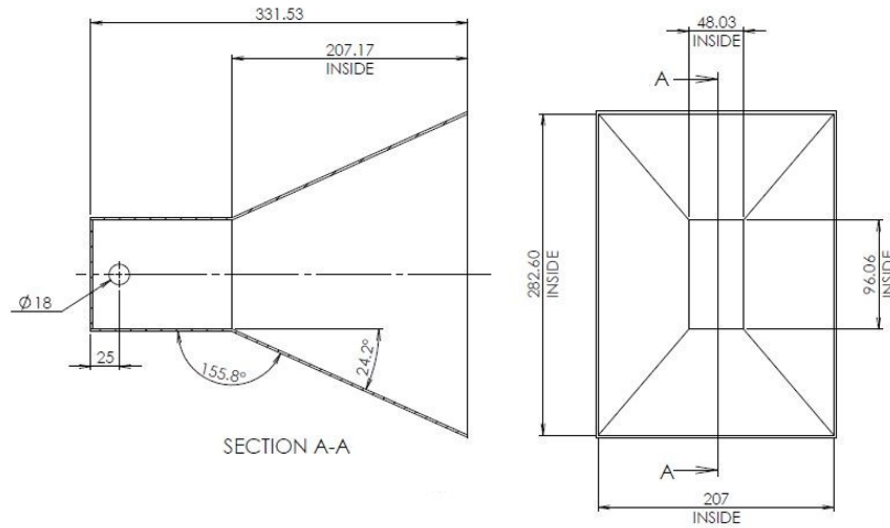
(a) Increase in gain.



(b) S_{11} .

Figure 15. The reflection coefficient and gain of the horn antenna after increasing its flare length.

Figure 16a shows the design of the pyramidal horn antenna, while the photo in Figure 16b shows a lab-built pyramidal horn antenna. The antenna was fabricated using A1110 aluminum and had dimensions of $W_a = 253.64$ mm and $H_a = 183.18$ mm, with metal thickness of 2 mm.



(a) Design of horn antenna.



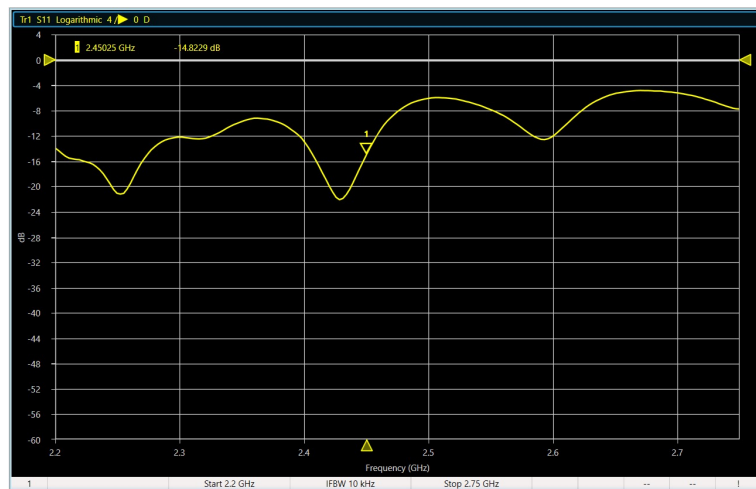
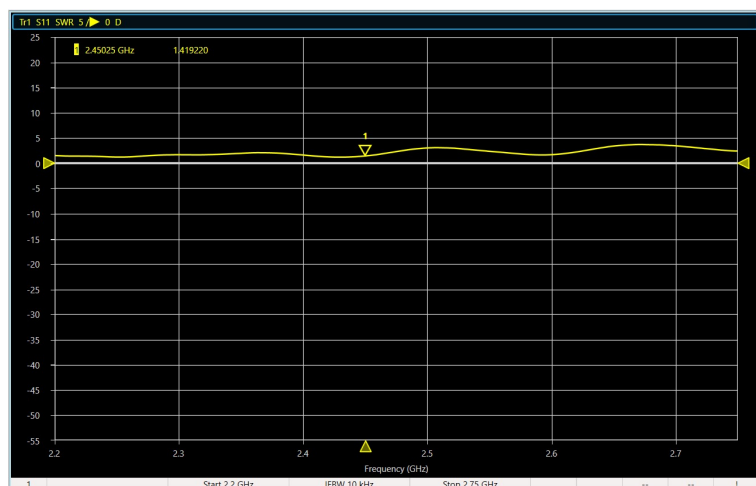
(b) Horn antenna made by welding aluminum sheets of 2 mm in thickness.

Figure 16. Design and fabrication of pyramidal horn antenna.

After the simulation and fabrication of the antenna, we tested it using Tektronix TTR506A. The setup for the measurement is illustrated in Figure 17a. The reflection coefficient (S_{11}) of the horn antenna was -14.83 dB at 2.45 GHz, as illustrated in Figure 17b. Figure 17c highlights a respectable VSWR of 1.42. The input impedance at resonant frequency was $Z = Z_0(1.015 + i0.34) = 49.25 + i17.12 \Omega$, as observed in Figure 17d.

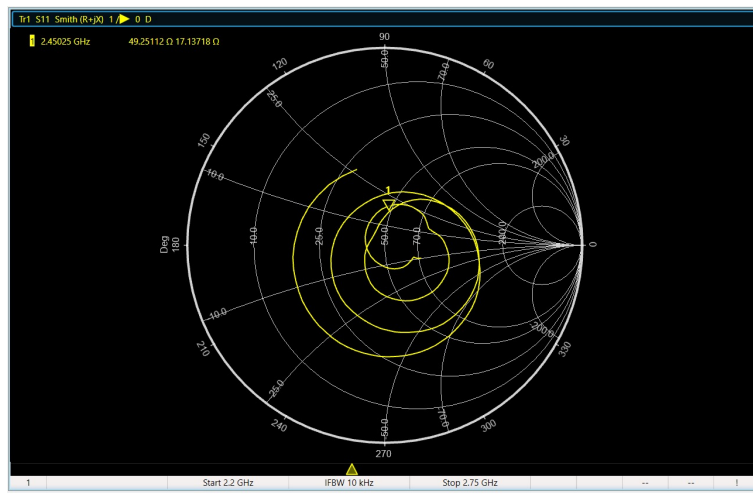


(a) Setup.

(b) S_{11} .

(c) VSWR.

Figure 17. Cont.



(d) Smith chart.

Figure 17. Measuring the pyramidal horn antenna.

A comparison of the transmitting horn antenna parameters between simulated and measured values can be found in Table 3. We fabricated the horn antenna using a waterjet cutting machine and a laser welding machine. Welding errors may have led to differing simulated and measured values of the horn antenna since welding was performed by hand.

Table 3. Comparison of horn antenna parameters.

	S ₁₁ in dB		VSWR		Gain in dB	
	Simulated	Measured	Simulated	Measured	Simulated	Measured
Horn antenna	−23.28	−14.82	1.10	1.41	14.5	12.33

Following the tests, we injected microwave energy into the waveguide by coupling it to the magnetron. In general, the waveguide carries the electric field lines generated by the antenna into space when attached to a horn antenna. At a given location in space, the resultant electric fields are

$$E = \sqrt{E_Y^2 + E_Z^2} \quad (13)$$

During RF transmission, magnetrons require a cooling system to increase efficiency. In the following subsection, we will explore the RF power budget. By estimating and calculating wireless transmission power loss, the Tx parameters can be calculated.

2.2. RF Power Budget

A transmitting antenna (TX) emits power density $W_t(\theta_t, \phi_t)$ in direction (θ_t, ϕ_t) . Power density is related to the transmitting horn antenna gain ($G(\theta_t, \phi_t)$), the power of the transmitter (P_t) fed to it, and the distance (D) between the transmitter point and the harvester circuit as follows [37]:

$$W_t = \frac{P_t}{4\pi R^2} G_t(\theta_t, \phi_t) \quad (14)$$

$$\text{FSPL} = 20\log_{10}(f) + 20\log_{10}(D) + 20\log_{10}\left(\frac{4\pi}{c}\right) - G_t - G_r \quad (15)$$

$$\text{FSPL} = 58.07 \text{ dB}$$

where the following apply:

D = distance between emitter and receiver;

P_t = transmitter power;

FSPL = free space path loss;

G_t = gain of the transmitting horn antenna;
 G_r = gain of the receiving horn antenna.

The effective receiving and transmitting antenna area is used in this section to calculate the required transmitter power, as shown in Figure 18.

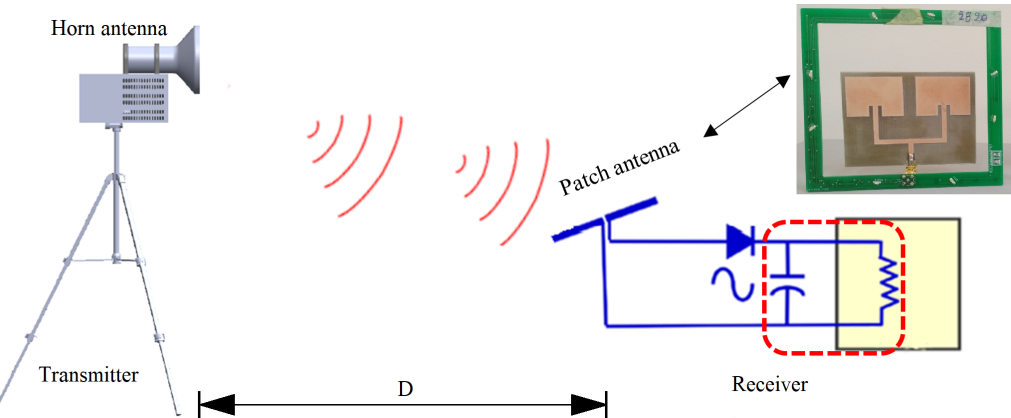


Figure 18. Diagram of a transmitting antenna and receiving antenna.

A twin-patch antenna's effective area on an ideal ground plane can be calculated using the following formula [38]:

$$A_{er} = \frac{G_r \lambda^2}{4\pi} \quad (16)$$

where the wavelength is

$$\lambda = \frac{c}{f} = \frac{3 \times 10^8}{2.45 \times 10^9} = 0.1223 \text{ m} \quad (17)$$

where G_r is the patch antenna gain and λ is the wavelength at 2.45 GHz. Based on Table 4, the gain was $G = 3.55 \text{ dBi}$. Based on Equation (16), the patch antenna had an effective area of 0.0023 m^2 . When a horn antenna transmits power over a distance (D), W_i can be expressed as follows [39]:

$$W_i = \frac{P_t G_r}{4\pi D^2} = \frac{P_t A_{et}}{\lambda^2 D^2} \quad (18)$$

where the following apply:

P_t represents the transmission power;

A_{et} represents the effective area of the pyramidal transmitting horn antenna;

D is the distance between transmitters and receivers.

The gain (G) of a pyramidal horn antenna is expressed as follows:

$$G = \left(\frac{\pi D_f}{\lambda} \right)^2 A_{er} \quad (19)$$

The aperture efficiency (A_{er}) is calculated as follows:

$$A_{er} = \left(\frac{\lambda^2}{4\pi} \right) G \quad (20)$$

$$\begin{aligned} A_{er} &= 0.0314 \text{ m}^2 \text{ (Horn Antenna)} \\ A_{er} &= 0.0026 \text{ m}^2 \text{ (Patch Antenna)} \end{aligned}$$

The effective area of a horn antenna equals its physical area (A) times its efficiency (E). A patch antenna receives power (P_r) as follows:

$$P_r = W_i A_{er} = \frac{P_t A_{et} A_{er}}{\lambda^2 R^2} \quad (21)$$

For maximum strength at the receiving point, Equation (21) shows the power demanded to transmit versus the distance gap between transmitting and receiving antennas. We assume that distance (D) lies within the antenna's far field. At close-in (reference) distances, the received power is expressed as follows:

$$P_{rx} = P_{tx}G_{tx}G_{rx}\left(\frac{c}{4\pi Df}\right)^2 \quad (22)$$

This subsection investigates how RF harvested power is influenced by the distance gap between an RF station and an emergency exit sign. The evaluation and comparison of simulation performance were performed using MATLAB. We used the MATLAB calculation platform to prove the above mathematical equations. Figure 19 shows the attenuation of RF energy versus the distance gap. Considering the range of the system is also important. The system should be able to transmit power over the desired distance.

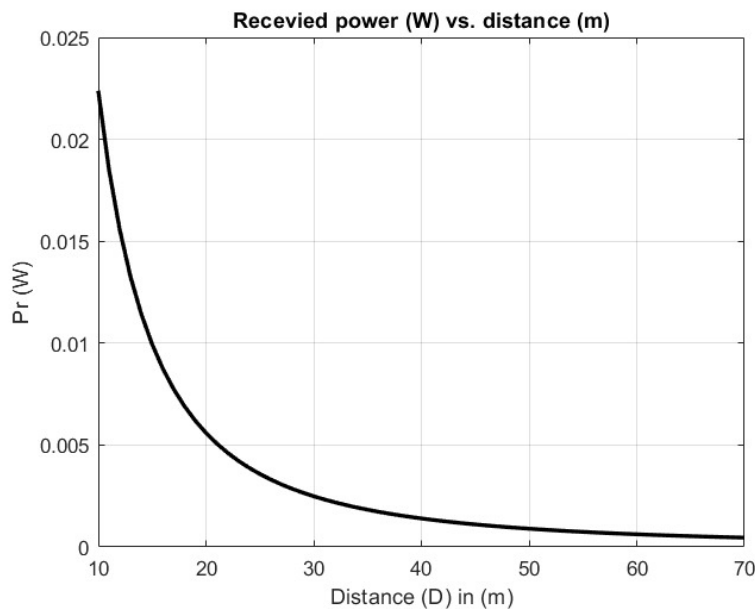


Figure 19. RF power received (W) vs. distance (m).

Based on Equation (22), the reflection-free propagation where the far field depends on the distance gap is $(1/D)$, while the power density decreases as $(1/D^2)$. The received power in dBm at close range is

$$P_{rx} = 10\log\frac{P_r}{0.001} \quad (23)$$

while the close-in received power in dBW is

$$P_{rx} (\text{dBW}) = 10\log\frac{P_r}{1W} = P_{rx} - 30 \quad (24)$$

Figure 20a–c depict received power (dBm), received power (dBW), and path loss, respectively, as functions of the distance (m). The increase in gap distance negatively impacts the received power.

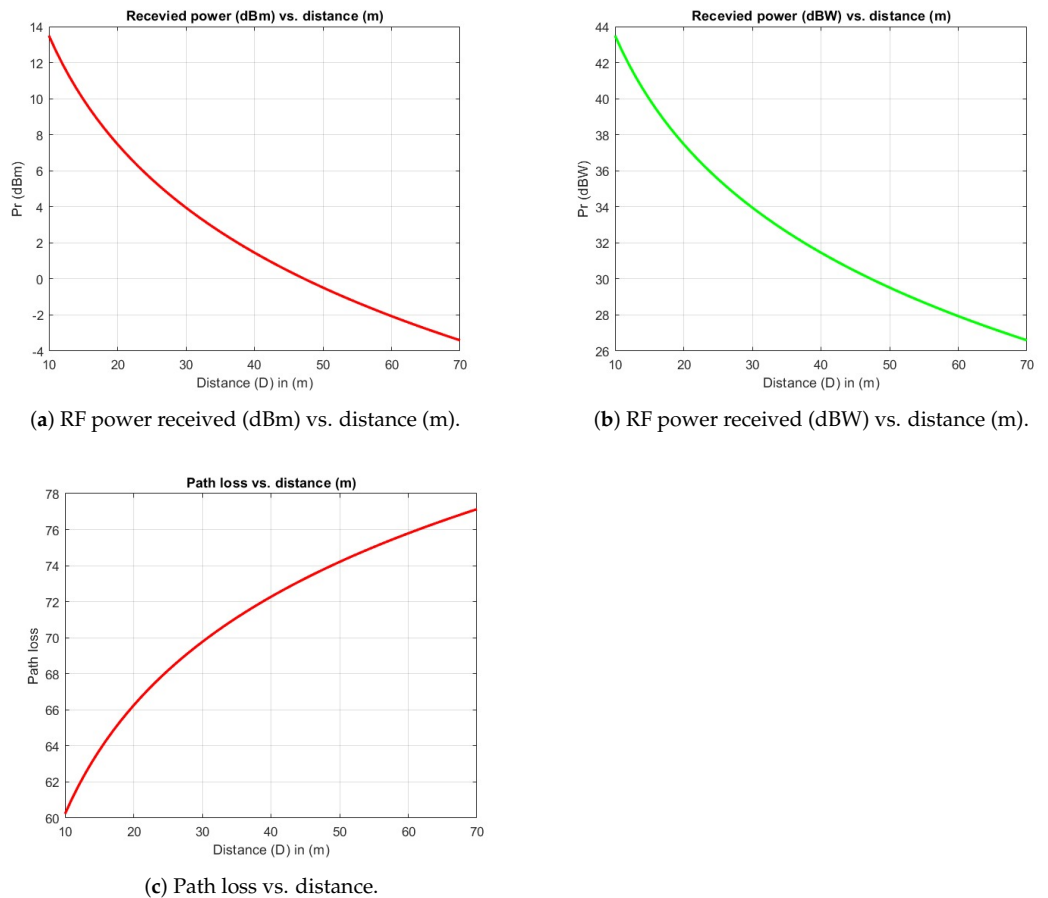


Figure 20. MATLAB simulation.

The reference power in dBm used to calculate the received power is

$$P_{rx} = P_r(\text{dBm}) + 20 \log\left(\frac{d_0}{d}\right) \quad (25)$$

The received power calculated using the reference power in dBW is

$$P_r(\text{dBW}) = P_r(\text{dBW}) + 20 \log_{10}\left(\frac{d_0}{d}\right) \quad (26)$$

Equation (27) represents the path loss:

$$P_L = \frac{P_t}{P_r} \quad (27)$$

3. Power Harvester Device

The RF rectifier circuit converts microwave energy into DC power. The circuit has four elements: a twin-patch antenna, a matching circuit, a rectifier circuit, and a voltage regulator. This subsection discusses each component of the RF harvesting system, as shown in Figure 21.

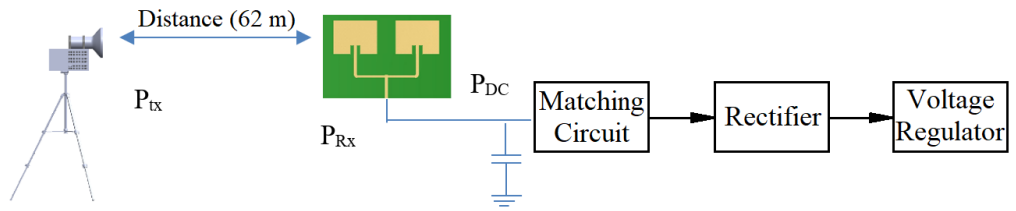


Figure 21. RF harvesting circuit block diagram.

3.1. Twin-Patch Antenna

The twin-patch antenna was engraved on an FR-4 substrate with thickness $h = 1.6$ mm, dielectric constant $\epsilon_r = 4.6$, and loss tangent $\delta = 0.02$. This structure was influenced by the twin-patch antenna published in our previous work [40,41] and similar works [42]. This work aims to increase the bandwidth of this antenna without increasing its occupied area or fabrication costs. The application requires a small, thin, cheap, and very compact RF energy harvester circuit with emergency exit lighting. Array patch antennas are ideal for this application due to their flexibility and size [43], and radiation strength determines the feed efficiency of harvester patch antennas. As presented in this section, we aimed to design, simulate, fabricate, and analyze a twin-patch antenna operating at 2.45 GHz. The proposed twin-patch antenna layout is illustrated in Figure 22a, while its substrate design is highlighted in Figure 22b.

The width of the patch antenna, W , is determined using Equation (28):

$$W = \frac{c}{2f_r(\sqrt{\frac{\epsilon_r+1}{2}})} \quad (28)$$

According to Equation (28), ϵ_r reduces the dimension of the antenna patch. We can calculate the actual patch length using Equation (29):

$$L = \frac{c}{2f_r\sqrt{\epsilon_{ref}} - 2\Delta L} \quad (29)$$

Based on Equation (29), the effective dielectric constant, ϵ_{ref} , is expressed as in Equation (30):

$$\epsilon_{ref} = \left(\frac{\epsilon_r + 1}{2}\right) + \left(\frac{\epsilon_r - 1}{2}\right) + \left(1 + \frac{12h}{W}\right)^{-1/2} \quad (30)$$

Furthermore, the length extension, ΔL , is calculated as described in Equation (31):

$$\Delta L = 0.412h \left[\frac{\epsilon_{ref} + 0.3}{\epsilon_{ref} - 0.258} \right] \left[\frac{\frac{W}{h} + 0.264}{\frac{W}{h} + 0.8} \right] \quad (31)$$

Then, the patch synthesis, H , with characteristic impedance Z_0 equal to 50 Ω is generated using Equation (32):

$$H = \left[\frac{Z_0 \sqrt{2(\epsilon_r + 1)}}{119.9} \right] + \frac{1}{2} \left[\frac{\epsilon_r - 1}{\epsilon_r + 1} \right] \left[\ln\left(\frac{\pi}{2}\right) + \frac{1}{\epsilon_r} \ln\left(\frac{4}{\pi}\right) \right] \quad (32)$$

Based on Equation (32), the width of the microstrip line feed, W_f , is computed as in Equation (33):

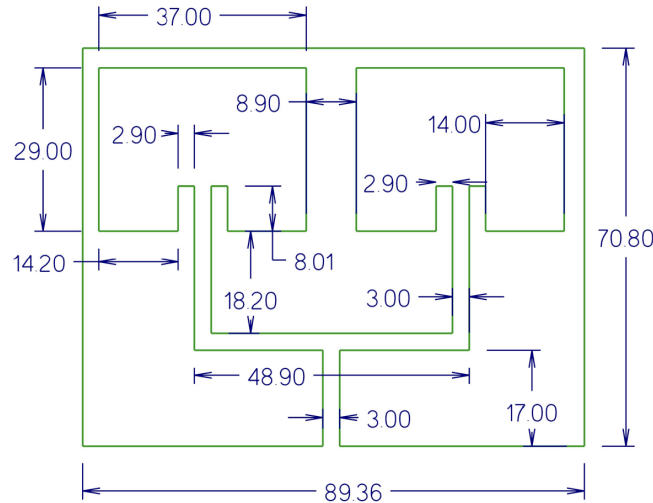
$$W_f = \left[\left(\frac{e^H}{8} - \frac{1}{4e^H} \right)^{-1} \right] \times 1.60 \text{ mm} \quad (33)$$

Moreover, the length of the microstrip line feed, L_f , is determined with Equation (34):

$$L_f = \theta \times \frac{\lambda_g}{360^\circ} \quad (34)$$

where

$$\lambda_g = \frac{c}{f\sqrt{\epsilon_{ref}}}$$
 (35)



(a) Dimensions of the twin-patch antenna.



Substrate Layer Stackup				
Type	Name	Material	Thickness	
Dielectric		AIR		
1 Conductor Layer	cond (4)	PERFECT_CONDUCTOR	0.34 um	
Dielectric		FR_4_Core	1.6 mm	
Cover		PERFECT_CONDUCTOR	0.35 um	

(b) Substrate of the twin-patch antenna.

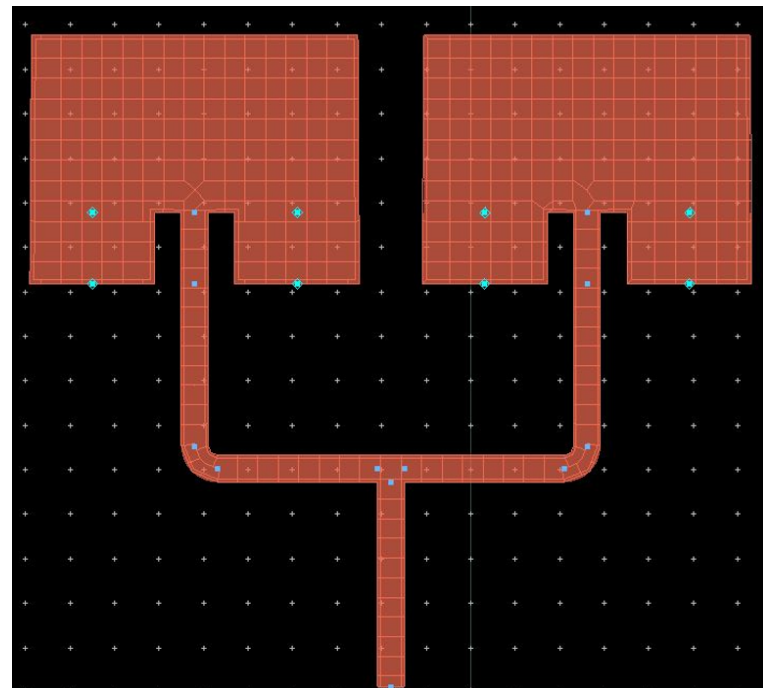
Figure 22. Proposed twin-patch antenna design.

The ground plane dimensions of this patch antenna are as follows:

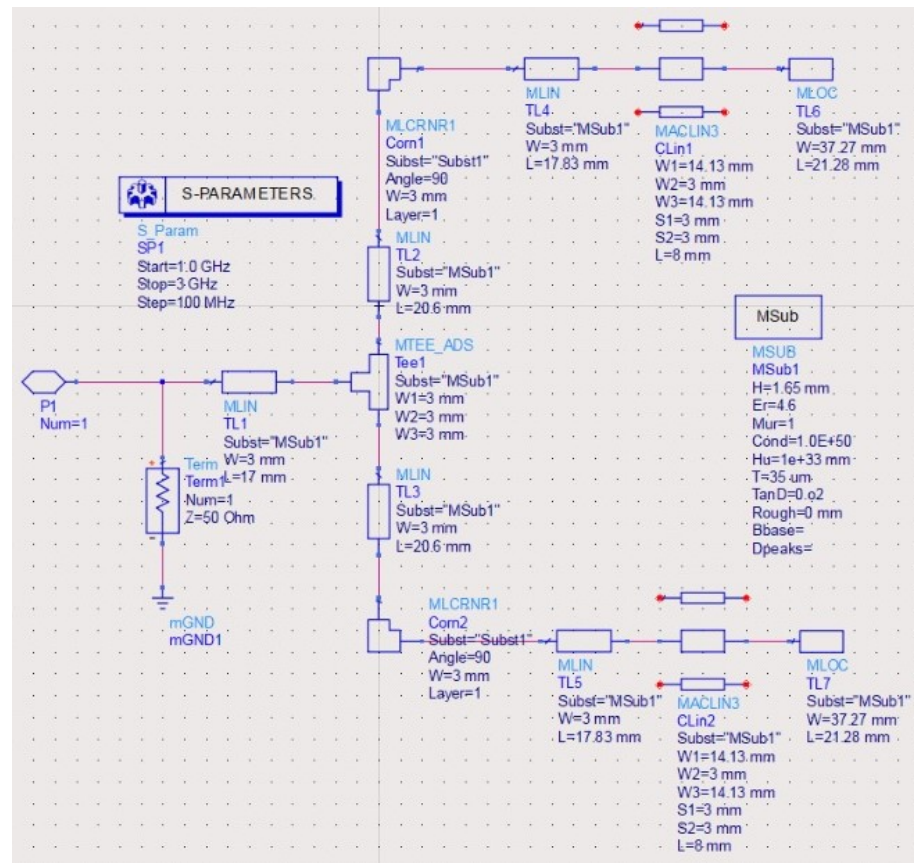
$$L_g = 6h + l$$
 (36)

$$W_g = 6h + w$$
 (37)

Therefore, the calculated L_g and W_g are 89.36 mm and 70.80 mm, respectively. As illustrated in Figure 23a,b, the twin-patch antenna dimensions were calculated and simulated with Advanced Design System (ADS) software. EEsof EDA, a unit of Agilent Technologies, produces Agilent Design System (ADS).



(a) Twin-patch antenna design in ADS layout.



(b) Twin-patch antenna design in ADS schematic.

Figure 23. Twin-patch antenna design.

At 2.453 GHz, the designed patch antenna has gain of 3.437 dBi and directivity of 7.814 dBi, as illustrated in Figure 24a,b, respectively. The relative bandwidth is greater than 1%. At an operating frequency of 2.453 GHz, the return loss is acceptable, $S_{11} = -19.69$ dB, as illustrated in Figure 25. At 2.453 GHz, the designed patch has a VSWR equal to 1.056 with a bandwidth of approximately 43 MHz. The frequency of 2.453 GHz shows high match impedance between the antenna and signal source without an imaginary impedance part. This results in accurate signal transmission. $Z = Z_0 \times (0.98 + i0.01) = 49 + i0.5 \Omega$.

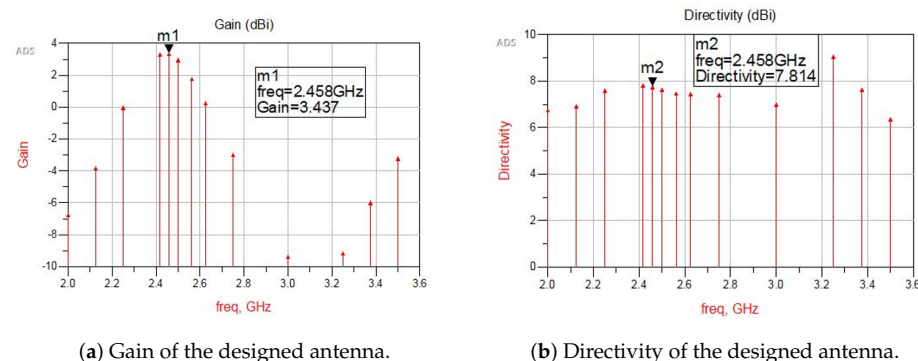


Figure 24. Gain and directivity of the designed antenna.

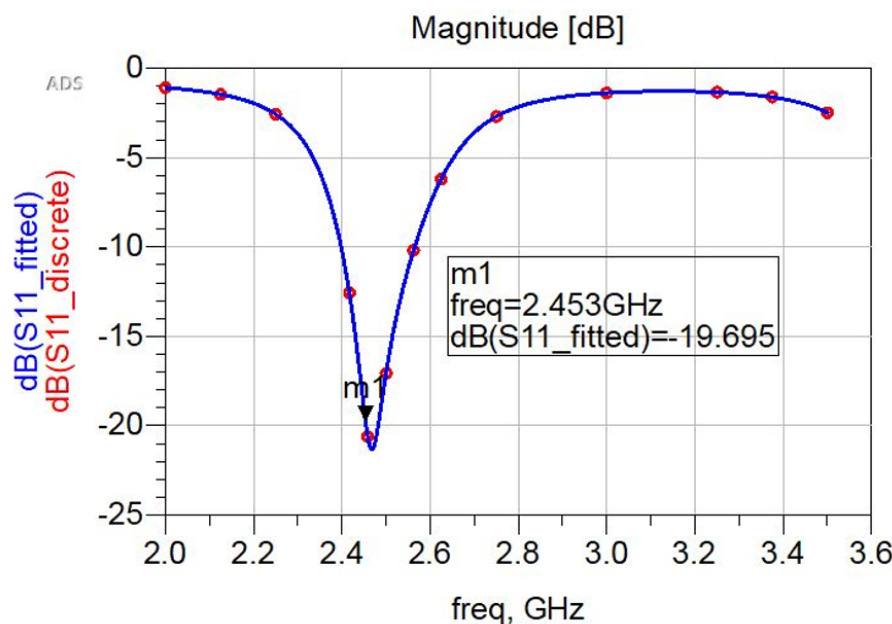


Figure 25. Simulated patch antenna reflection coefficients.

The twin-patch antenna current distribution graph is shown in Figure 26; we see that at and near the feed, the magnitude of the current distribution is minimized due to a change in antenna impedance. Variations in the current distribution contribute to antenna performance parameters.

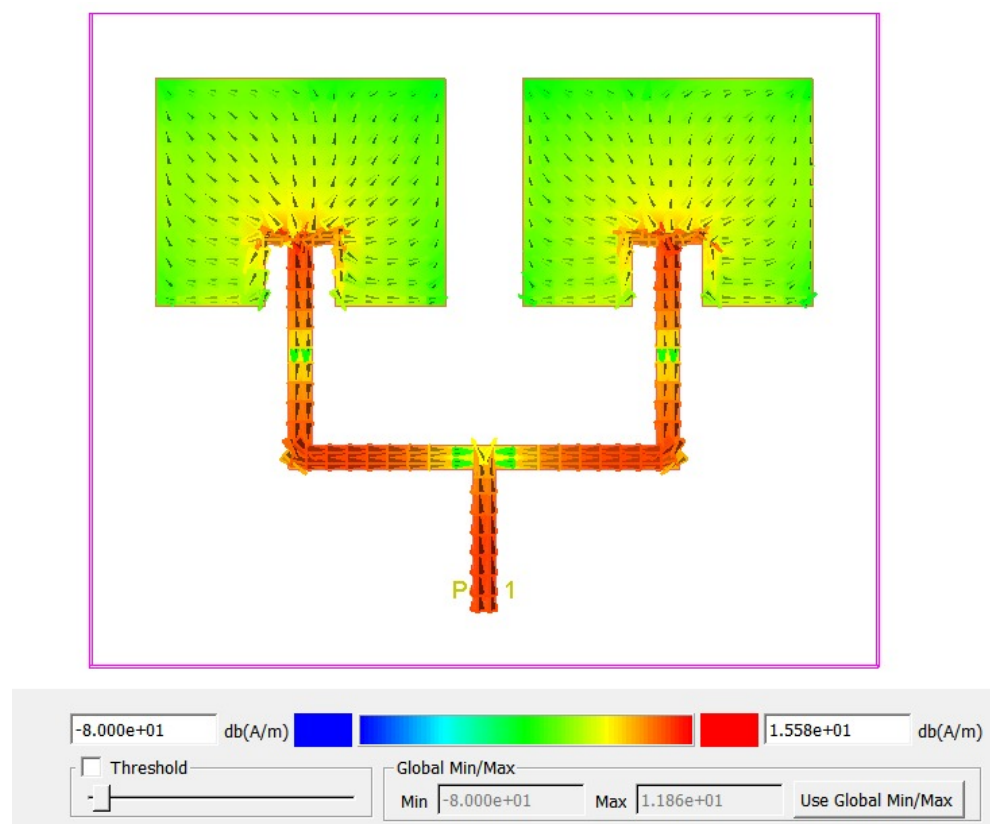


Figure 26. Simulation of the current distribution.

Figure 27 illustrates the radiation pattern of the twin-patch antenna derived from the simulation. Both the E-plane and H-plane are shown. The gain of 3.7 dB is achieved by the patch antenna at 2.45 GHz.

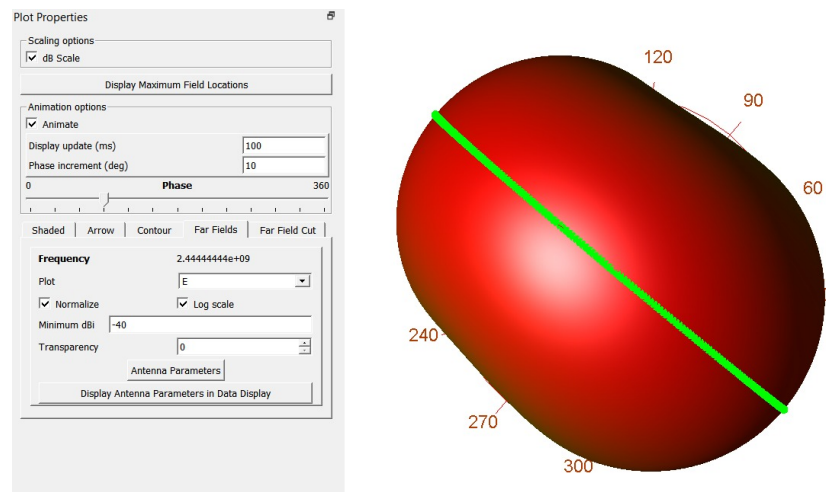
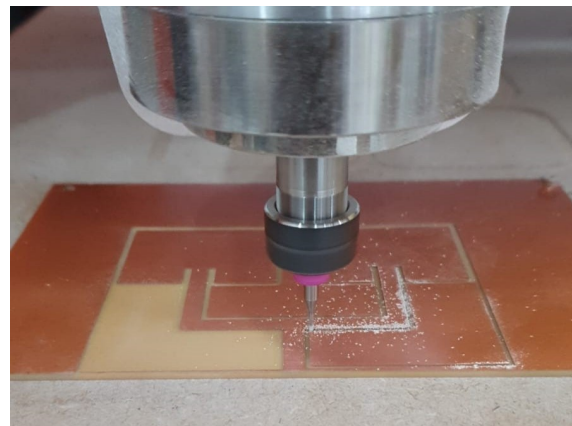
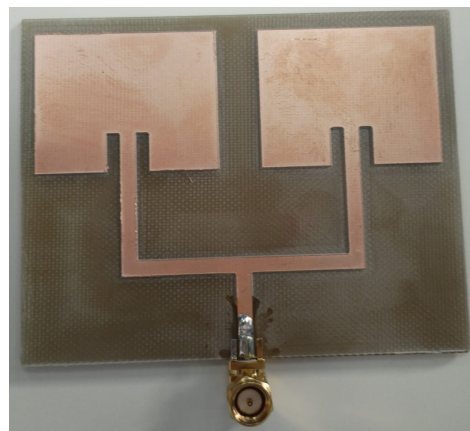


Figure 27. Gain plot of the twin-patch antenna.

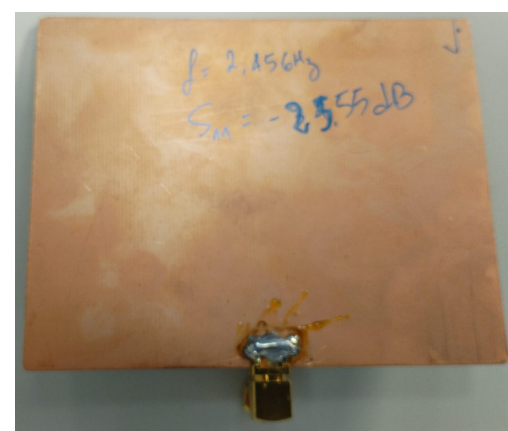
This antenna was simulated with ADS keysight software and fabricated using the engraving CNC technique, as shown in Figure 28a. The top view of the realized antenna is illustrated in Figure 28b, and the bottom view is illustrated in Figure 28c.



(a) Fabrication of twin antenna.



(b) Top view.



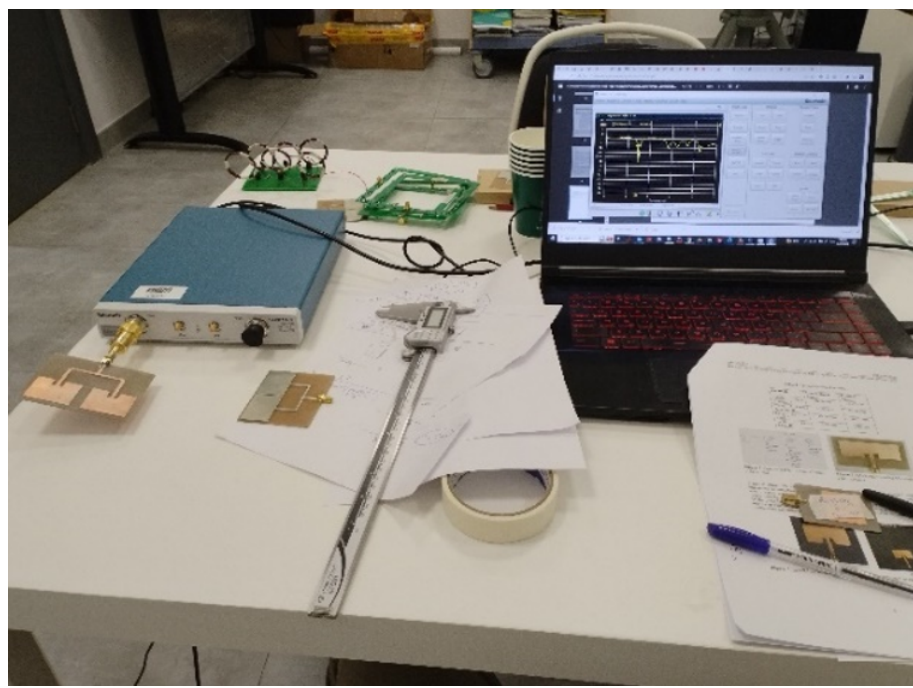
(c) Bottom view.

Figure 28. Fabricated microstrip twin-patch antenna.

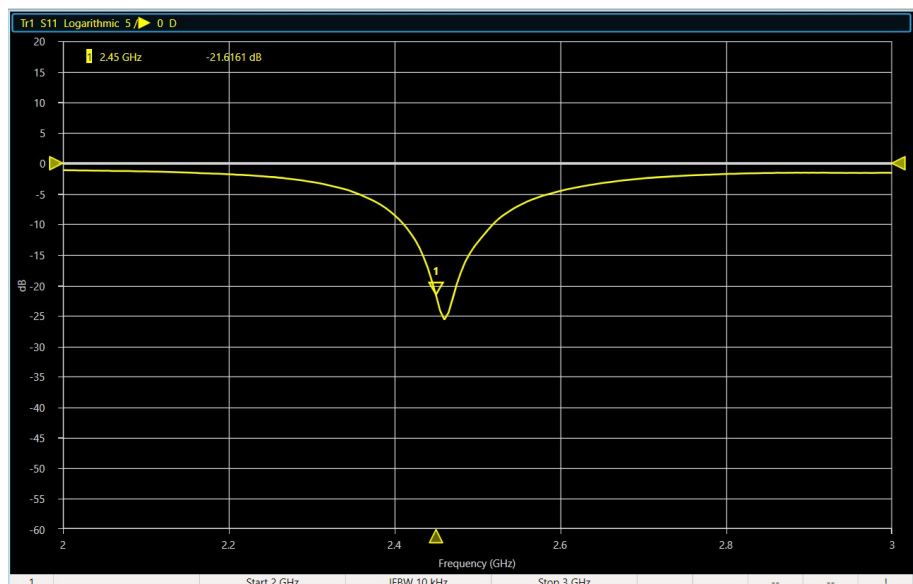
There is no doubt that this antenna has acceptable performance in theory. We tested the antenna using (VNA) TTR506A. The setup for the measurement is shown in Figure 29a, and the results are shown in Figure 29b. The antenna resonated at 2.45 GHz with a reflection coefficient (S_{11}) of -21.66 dB, while the theoretical simulation value was -19.69 dB. At 2.45 GHz, this antenna is highly efficient. Thus, the patch antenna has a bandwidth from 2.43 GHz to 2.57 GHz at $S_{11} < -10$ dB.

Figure 30 shows the VSWR of the fabricated twin antenna. The VSWR is 1.17, which is an acceptable value. The VSWR and return loss of the fabricated antenna are lower, which means that the patch antenna has low return loss.

The tested value of the twin-patch antenna input impedance at resonant frequency was $50.21 + i2.35$. The tested and simulated input impedance values are close, as shown in Figure 31a,b.



(a) Setup.



(b) Results.

Figure 29. Measuring twin-patch antenna parameters.

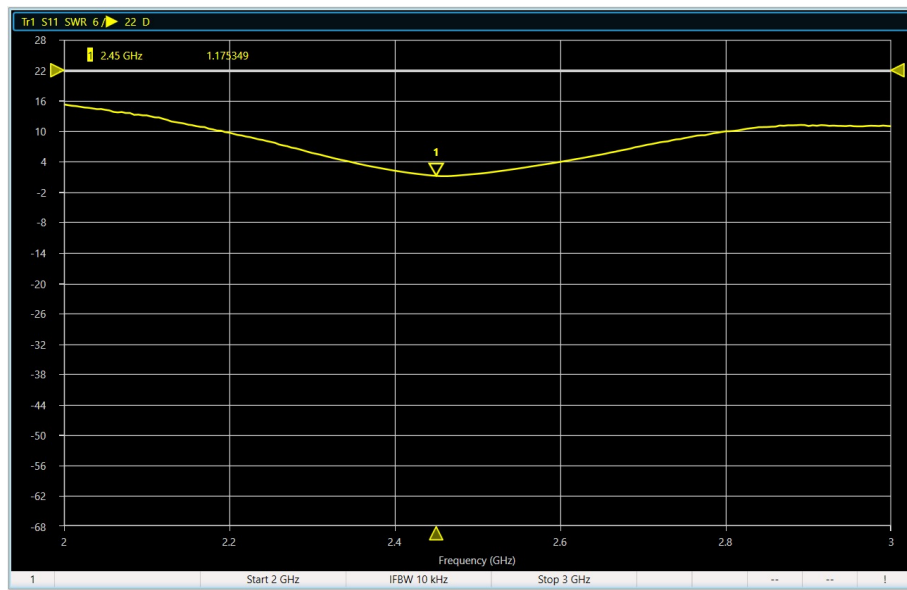


Figure 30. VSWR measurement value.

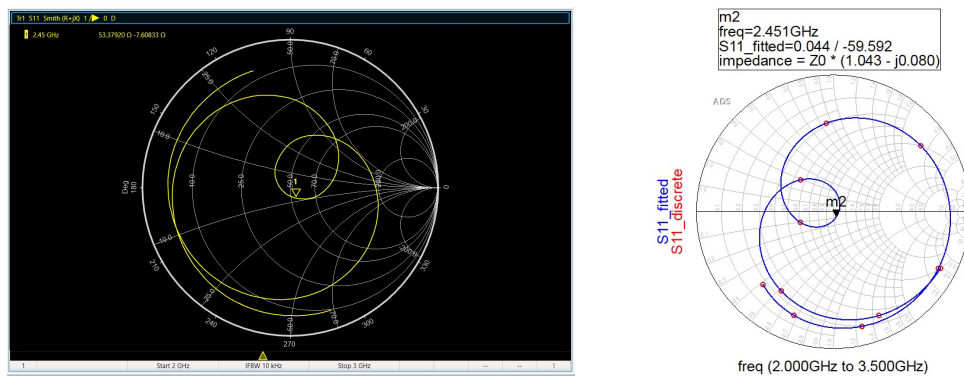


Figure 31. Twin-patch antenna impedance.

So, this antenna provides a much better match at 2.45 GHz, with minor reflection. The maximum gain of a receiving antenna is 3.210 dB. A comparison of the harvester patch antenna parameters between simulated and measured values can be found in Table 4.

Table 4. Comparison of patch antenna parameters.

	S ₁₁ in dB		VSWR		Gain in dB	
	Simulated	Measured	Simulated	Measured	Simulated	Measured
Patch antenna	-19.65	-21.66	1.21	1.17	3.437	3.55

The patch antenna is highly omnidirectional and has a small BW, low return loss, and a low VSWR close to one. The slight differences between the measured value and the simulated values are probably due to the fabrication process. We used a CNC router machine for PCB etching. The slightest errors in alignment can lead to unintended changes in the final design and to the VSWR and S_{11} parameter being inaccurate. Our next step was to examine the rectifier harvester circuit after the twin-patch antenna had been simulated, fabricated, and validated.

3.2. Rectifier Investigation

The construction of RF/DC converters is discussed here, beginning with selecting and analyzing the components according to the output voltage and current desired. This paper presents the performance of a high-frequency rectifier harvesting circuit composed of Schottky diodes with varying characteristics.

Most researchers in this field look for a reflection coefficient of less than -10 dB in the prototype to evaluate whether the matching impedance is acceptable and reasonable [44]. We aimed to reduce reflection loss by matching impedance and converting an external power. The first step to improving RF harvesting circuit performance is to reduce reflection loss [45,46]. Agilent ADS includes a Smith chart matching tool to synthesize a CL filter for matching impedance. Figure 32 shows the matching network topology, with inductance L in series ($L = 1.10$ nH) and capacitor C in shunt ($C = 9.31$ pF). The tuning procedure is complex. In order to find the real part of the impedance equal to 50Ω , the ADS Smith chart simulator was used to tune the LC filter values, as shown in Figure 33a.

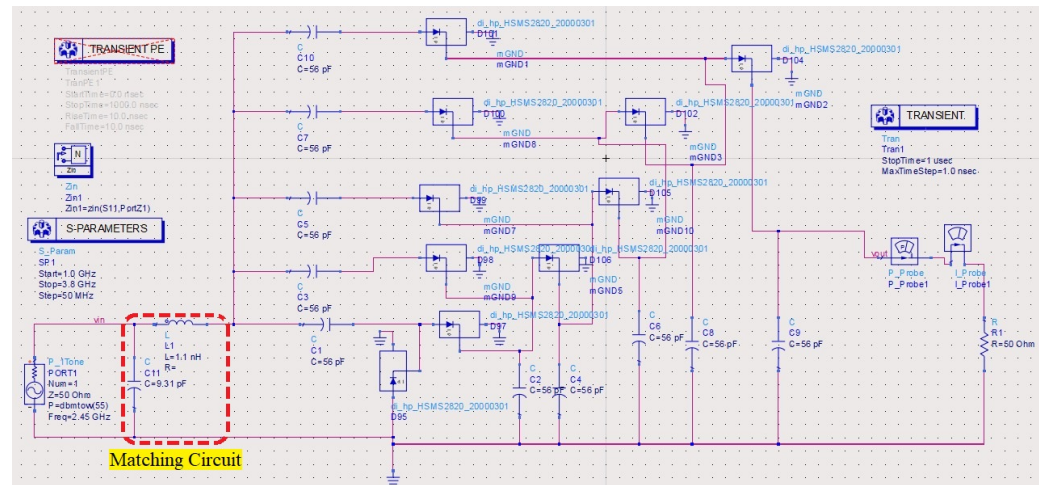


Figure 32. An RF harvesting circuit using a five-stage voltage multiplier (Agilent ADS).

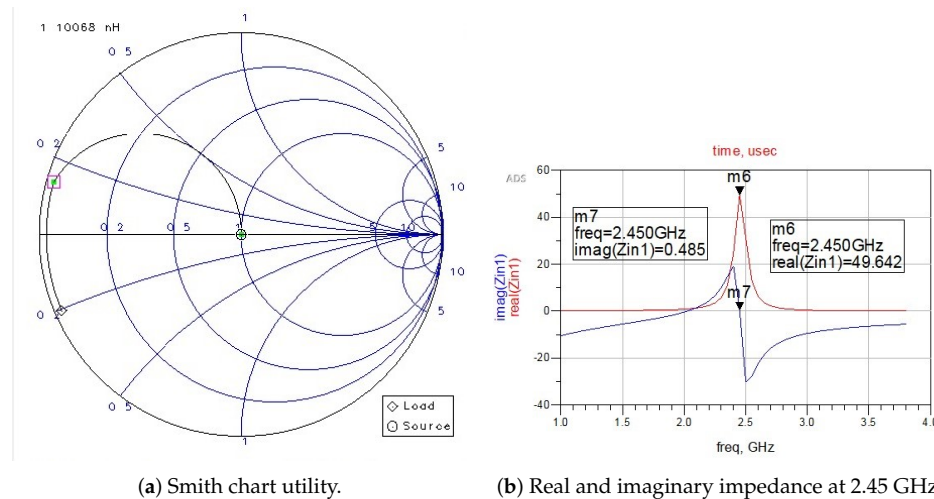


Figure 33. Cont.

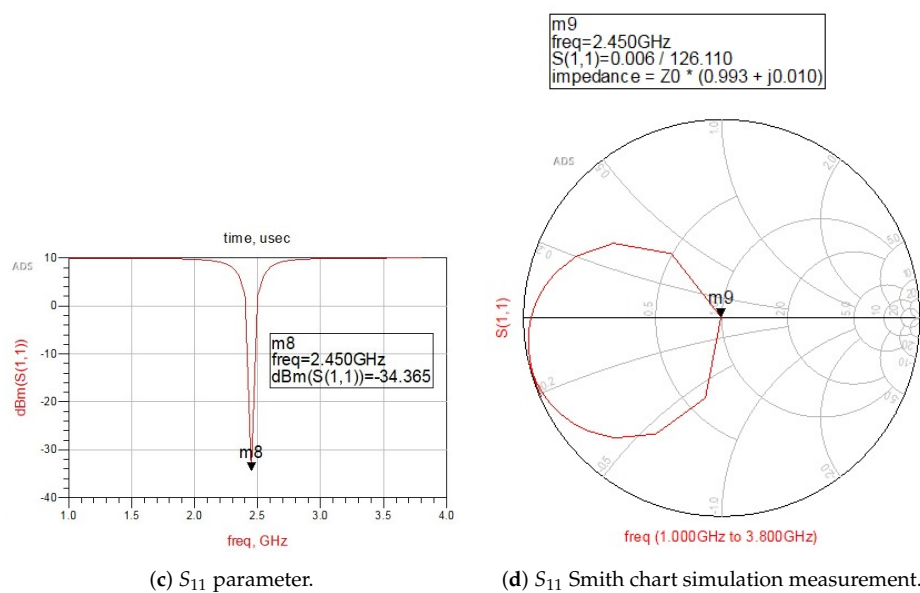


Figure 33. Impedance matching.

The RF rectifier was matched to 2.45 GHz with the real part at 49.64Ω and the imaginary part at 0.485 , as shown in Figure 33b. The matching network overcame the approximately 4% power loss in the model due to an impedance mismatch between the antenna and rectifier. The S-parameter (SP) simulator is highly recommended for simulating reflection coefficient S_{11} and input impedance. This rectenna resonated at 2.45 GHz with a reflection coefficient (S_{11}) of -34.36 dB, as shown in Figure 33c. As shown in Figure 33d, the measured impedance is

$$Z = Z_0(0.993 + j0.01) = 49.65 + j0.5\Omega. \quad (38)$$

Figure 34a highlights the setup for rectifier impedance measurement. Figure 34b illustrates the measured return loss response of the converter circuit. The twin-patch antenna and rectifier were impedance-matched using a CL impedance-matching circuit. The CL section consisted of a 1.10 nH inductor and a 9.31 pF capacitor in a parallel-series configuration. At 2.45 GHz, this CL circuit matches the twin-patch antenna impedance of $49.5 - j18.20 \Omega$ to the rectifier circuit impedance of $3.03 - j16.808 \Omega$. In addition to passing RF energy at 2.45 GHz, the CL filter circuit eliminates unnecessary higher-order harmonics and reduces reflection loss.

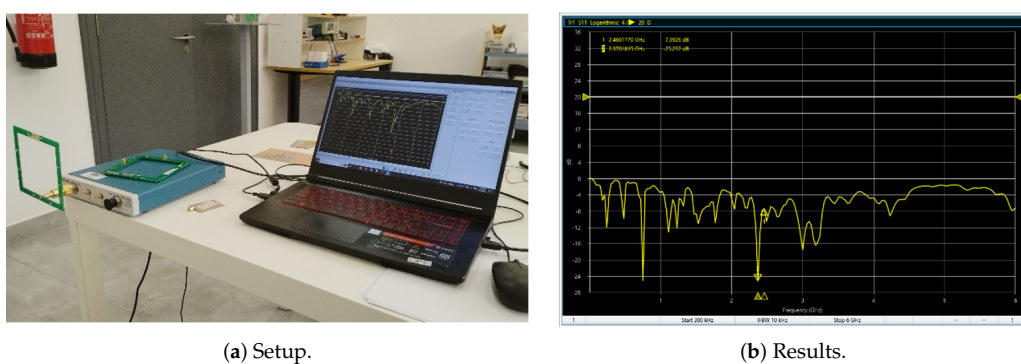


Figure 34. RF/DC rectifier circuit impedance measurement.

Diode selection in this type of application is critical because the circuit requires a 2.45 GHz RF frequency. Diodes should operate within the frequency band; otherwise, the

circuit does not work correctly. For the rectifier circuit, four different RF Schottky diodes were used (HSMS2820, HSMS2810, HSMS2810, and BAS40-04). The electrical specifications of these diodes are highlighted in Table 5.

Table 5. Electrical specifications of the diodes.

Diode	Minimum Breakdown Voltage V_{BR} (V)	Maximum Forward Voltage V_F (mV)	Maximum Reverse Leakage Current I_R (nA)	Maximum Capacitance C_T (pF)
HSMS2820	15 @ $I_R = 100 \mu\text{A}$	340 @ $I_F = 1 \text{ mA}$	100 @ $V_R = 1 \text{ V}$	1.0 @ $V_F = 0 \text{ V}$, $f = 1.0 \text{ MHz}$
HSMS2810	20 @ $I_R = 10 \text{ mA}$	410 @ $I_F = 1 \text{ mA}$	200 @ $V_R = 15 \text{ V}$	1.2 @ $V_F = 0 \text{ V}$, $f = 1.0 \text{ MHz}$
HSMS2804	70 @ $I_R = 10 \text{ mA}$	410 @ $I_F = 1 \text{ mA}$	200 @ $V_R = 50 \text{ V}$	2.0 @ $V_F = 0 \text{ V}$, $f = 1.0 \text{ MHz}$
BAS40-04	40 @ $I_R = 10 \mu\text{A}$	380 @ $I_F = 1 \text{ mA}$	200 @ $V_R = 30 \text{ V}$	5.0 @ $V_R = 0 \text{ V}$, $f = 1.0 \text{ MHz}$

From 0.1 to 9 GHz is the frequency range of these diodes. Table 6 shows the impedance-matching measurements with different diodes for an RF/DC rectifier circuit.

Table 6. Measurement of the RF/DC rectifier circuit impedance matching.

RF/DC Rectifier Diode Types	S_{11} Return Loss (dB) at 2.45 GHz
HSMS2820	-9.03
HSMS2810	-7.43
HSMS2804	-3.41
BAS40-04	-5.45

A five-stage voltage multiplier with the HSMS-2820 diode was used in this work to harvest RF signals. The second stage of a single doubler circuit receives only the noise of the first stage. This noise is doubled and added to the DC voltage of the first stage in the second stage. The system should produce more voltage regardless of the input by adding more stages [47]. A voltage multiplier circuit dedicated to each independent stage consists of a micro cell with open circuit output voltage V_0 , load resistance R_L , internal resistance R_0 , number of voltage multiplier stages n , and output voltage V_{out} . Based on this variation in R_L , V_{out} is calculated with Equation (39):

$$V_{out} = V_0 \left[\frac{1}{\frac{R_0}{R_L} + \frac{1}{n}} \right] \quad (39)$$

Using different Schottky diodes (HSMS2820, HSMS2810, BAS40-04, and HSMS804), we simulated a five-stage voltage multiplier until we reached the highest output voltage and current. The circuit used HSMS2820 Schottky diodes to harvest RF energy. The voltage gain decreased as the number of steps increased, whereas higher voltage was obtained as the number of steps increased. Further, 50Ω load resistance was applied to the parallel connection for the maximum output power test. Using HSMS2820 diodes, the DC output voltage obtained in a five-stage voltage multiplier simulation was 8.401 V, as shown in Figure 35a. The HSMS2820 family has high output voltages because of their low flicker noise and low junction capacitance. Figure 35b reports the output current of 0.169 A from the simulation.

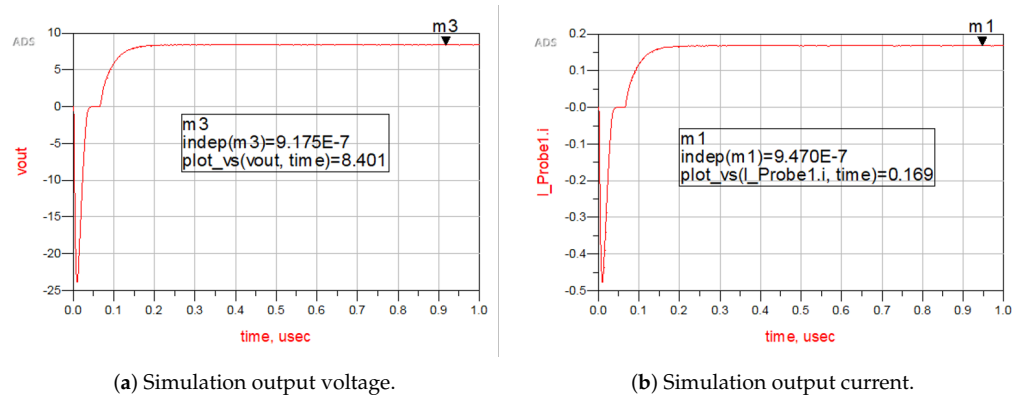


Figure 35. The simulation results after optimization (HSMS2820).

According to the simulation, the output power was equal to 1.422 W, as shown in Figure 36.

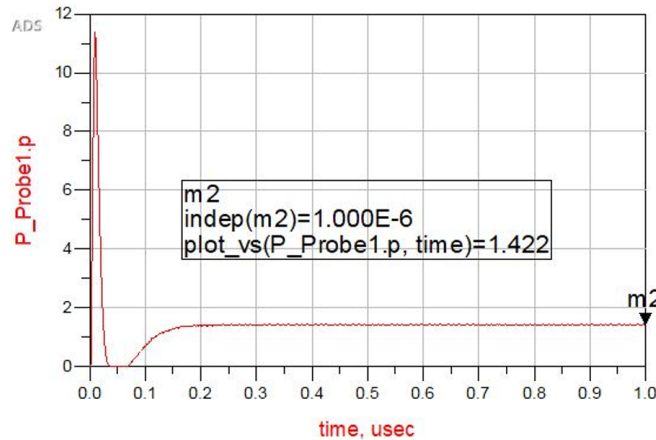


Figure 36. Output power of the rectifier circuit.

We used an RF frequency generator (the SMC100A, by Rohde & Schwarz, Munich, Germany) to test the efficiency of the rectifier at the operating frequency by coupling the RF/DC circuit to it. RF harvesting circuits operate in the 2.4 GHz to 2.6 GHz range, as illustrated in Figure 37.

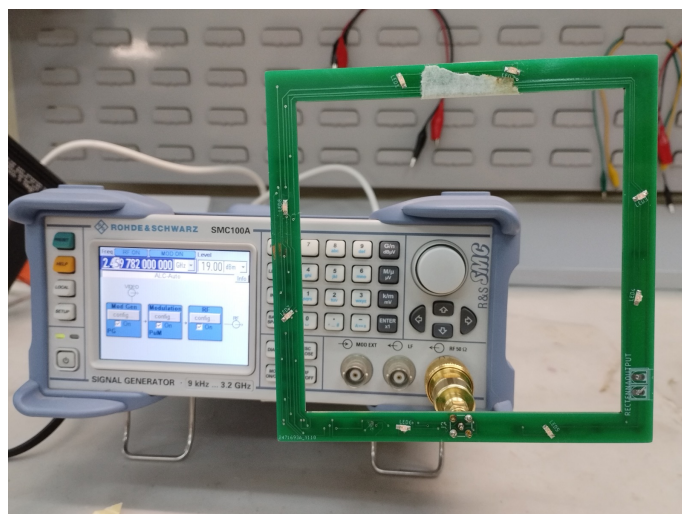


Figure 37. Frequency range measurement for rectifier circuit (HSMS2820).

Table 7 shows how the Schottky diodes changed the efficiency of the rectifier circuits.

Table 7. Measurement of RF/DC rectifier efficiency.

Diode	P_{in} (dBm)	Load Resistance Ω	V_{out} (V)	I_{out} (mA)	P_{out} (W)	Efficiency $\nu = (V_{out} \cdot I_{out}) / P_{in}$ (%)
HSMS2804	33	50	9.75	20	0.19	5.91
BAS40-04	33	50	2.00	4.12	0.0081	0.25
HSMS2820	33	50	3.86	8	0.03	0.93
HSMS2810	33	50	11.60	23	0.27	8.09

As a result of its low series resistance, low forward voltage at current levels, and superior RF characteristics, the HSMS28XX series is an excellent choice for RF scavenging. HSMS2820 detector diodes are zero-bias detectors designed for small-signal applications. HSMS2810 Schottky diodes, despite their apparent high series resistance, provide low RF rectifier power levels. Compared with HSMS2804, HSMS2810 diodes are approximately 11.6 times more efficient. HSMS2820 provided high output voltage in this test. Figure 38 shows the schematic circuit of an RF rectifier on a PCB.

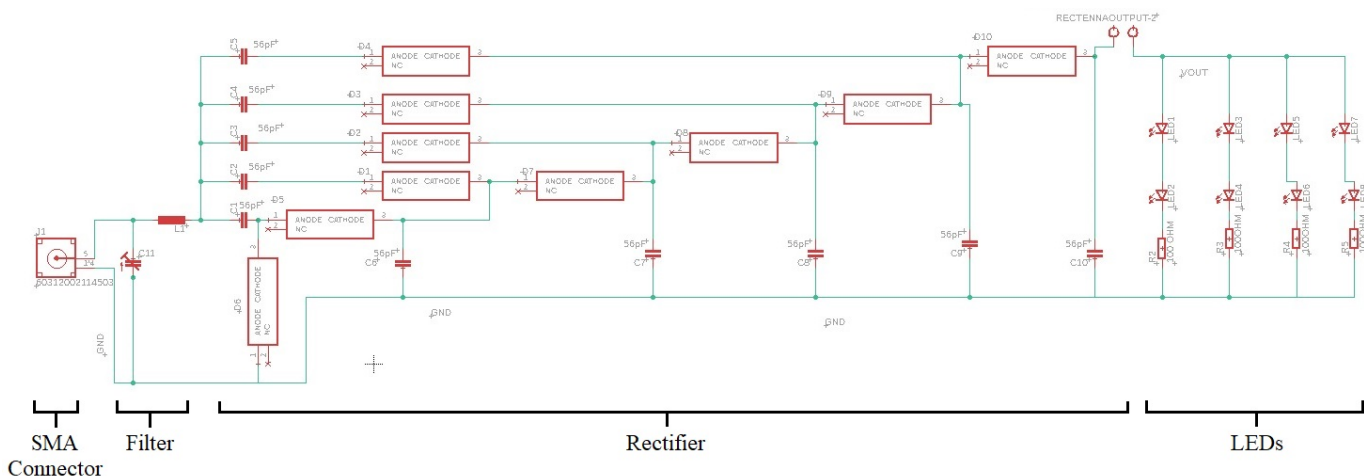


Figure 38. Rectifier PCB schematic circuit.

We constructed four rectifier circuit PCBs, each one had different Schottky diode parameters (HSMS2820, HSMS2810, HSMS2804, and BAS40-04), to evaluate the entire RF harvester circuit, as shown in Figure 39a,b. The prototype used was a red of 60 mW with high luminosity of 70 mcd manufactured by everlight, electronics, New Taipei City, Taiwan. These diodes require 2.4 V and 20 mA current to achieve high brightness.

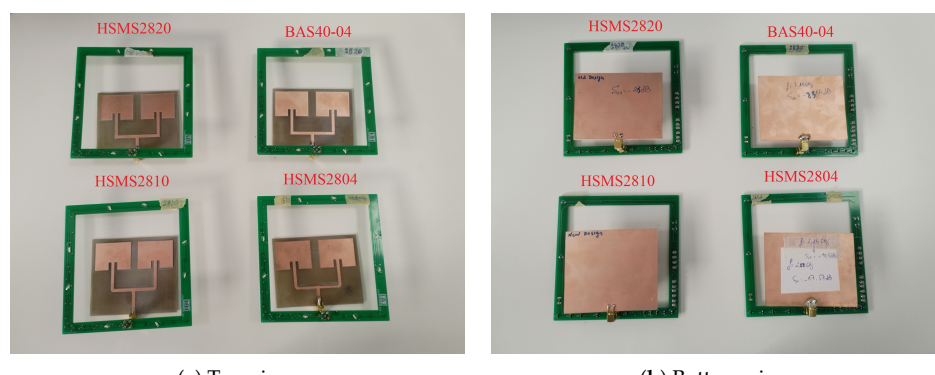


Figure 39. Fabricated four RF power harvesting PCBs with different Schottky diode types.

4. Prototype Results and Discussion

Portable microwave radiation stations operate at a frequency of 2.45 GHz and have a power output range of 500 W. RF energy converters calculate DC output levels using equations and assuming a direct line of sight between the patch and horn antennas. The wireless power efficiency determines the gain values of the Rx and Tx antennas. The patch length, width, ground length, width, substrate depth, thickness, and other parameters all contribute to the efficiency of wireless powering emergency lighting. Table 8 presents a summary of the simulation results.

Table 8. Parameters of receiving and transmitting antennas.

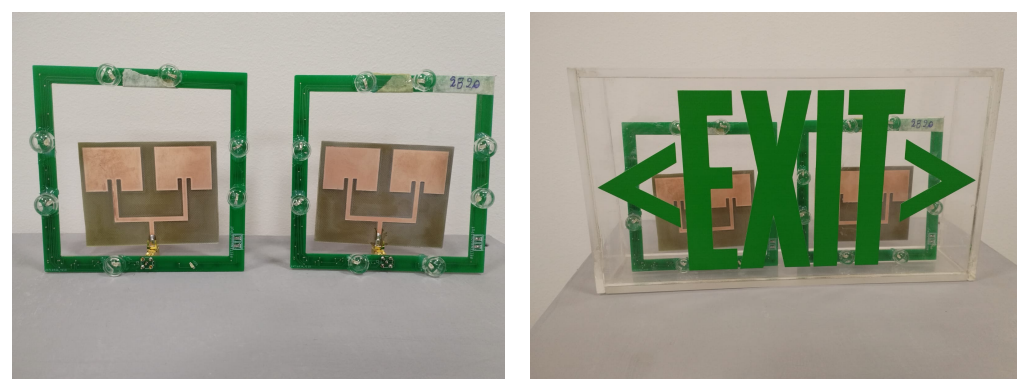
Parameter	Receiving Patch Antenna (Rx) Value	Horn Antenna (Tx) Value
Return loss	−21.66 dB	−14.82 dB
BW (GHz)	2.43 GHz to 2.58 GHz	2.33 GHz to 2.62 GHz
Gain (dB)	3.55	12.33
Directivity (dB)	7.9	11.03
VSWR	1.17	1.41

In this investigation, we used FR-4 substrate materials. We performed simulations for wireless applications at a 2.45 GHz operating frequency. According to the simulations, the receiving antenna gain was 3.55 dB; the directivity was 7.471 dBi; the return loss was −21.66 dB; the BW was 0.0746 GHz; the bear loss was 1.17; and the efficiency was 34.69%. The results were −12.542 dB return loss, gain of 8.09 dB, directivity of 8.587 dBi, accuracy of 0.0349 GHz, a VSWR of 1.617, and efficiency of 94.24% for the horn antenna, respectively. A patch antenna and HSMS2820 generated a maximum DC voltage of 8.401 V, with a current of 0.167 A. The antennas were in the line of sight (LOS) during lab testing from 1 m to 62 m. According to Table 9, power harvesting appeared to vary significantly with the distance from the microwave power station $P_{in} = 500$ W to the receiver circuit.

Table 9. Energy harvesting range vs. distance.

RF Transmitter Power (P_r)	Distance between RF Transmitter and Observation Point (m)	Harvested Energy (W)
500 W	5	4.19
500 W	15	2.79
500 W	25	2.3
500 W	45	1.2
500 W	60	0.483

We added a mini LED lens convex acrylic reflector with a 120-degree angle, as shown in Figure 40a,b, to better view the glow of the LEDs from a distance.



(a) Lenses added to the LEDs.

(b) Prepared circuit placed in the emergency exit sign.

Figure 40. Convex lens added to the exit sign.

Figure 41a shows the position and orientation of the transmitter and receiver at a distance of 5 m. The rectenna successfully harvested energy. Figure 41b,c highlight the same test at 10 and 25 m, respectively.



Figure 41. Energy harvesting tests at various distances.

Figure 42a,b show the setup for harvesting energy at a distance of 62 m at 1× and 100× zoom levels, respectively. This application should be mounted and installed at a higher level near the building ceiling, along with exit signs for safety precautions. It is a directed wave, so it would not affect people while evacuating.

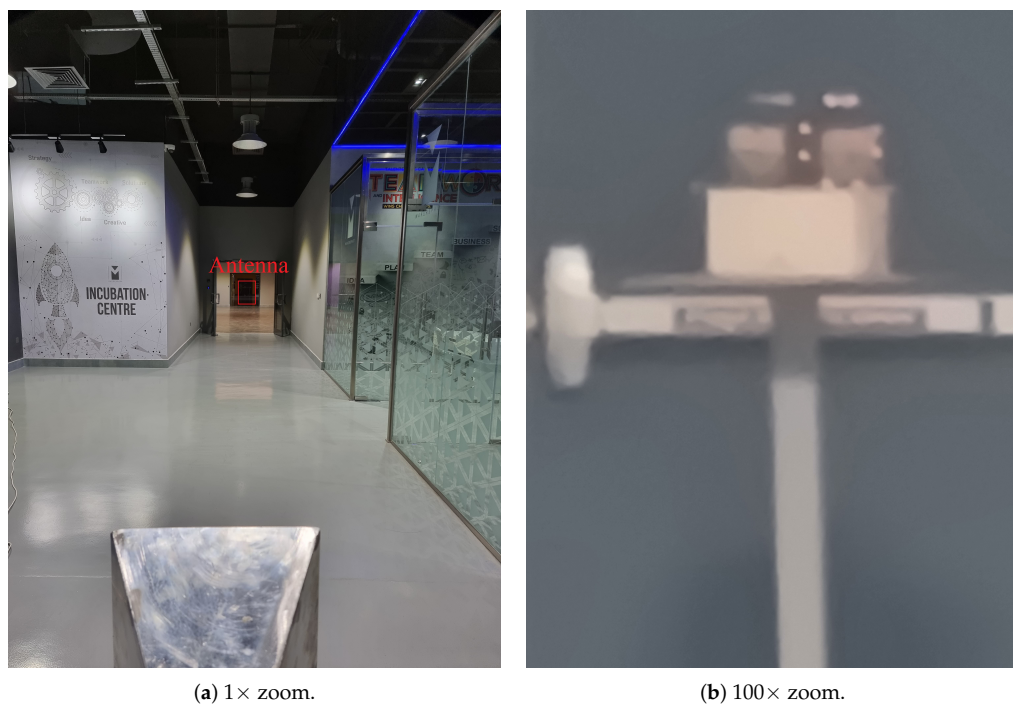


Figure 42. Photographs of the RF energy harvesting setup at a 62 m distance.

We could mount this solution in a building provided that there is no obstruction between the signs and the RF transmitter station, or we could make a portable RF power station that the building security team or civilian defense can use if the emergency signs fail. This device can only be used with signs within range so that it can charge many signs simultaneously without any obstacles.

Safety is one of the biggest challenges facing the system. A key component of this is ensuring that the system's power output is not too high. Our transmitter operates at 2.4 GHz. Microwaves are an example of non-ionizing radiation that do not directly affect the structure of atoms or damage DNA; however, they do cause atoms to vibrate, which can cause them to heat up [48]. The ability to heat up atoms is the reason microwaves are used for cooking in microwave ovens, which also operate at 2.4 GHz. The United States Food and Drug Administration (FDA) limits the amount of microwaves that can leak from an oven throughout its lifetime to 5 mW/cm^2 or $50,000 \text{ mW/m}^2$ of microwave radiation at approximately 2 inches from the oven surface [49]. This limit is far below the level known to harm people. We measured the radiation from our transmitter at a distance of 8 m using a Tektronix Real-Time Spectrum Analyzer and found it to be 155 mW/m^2 , as shown in Figure 43. This is much lower than the limit set by the FDA for microwave oven radiation leakage. Hence, unless someone is standing right in front of the transmitter or is exposed to the radiation for an extremely long time, the transmitter should be safe to use for emergency evacuations. More information can be found in Supplementary Materials Video S2.

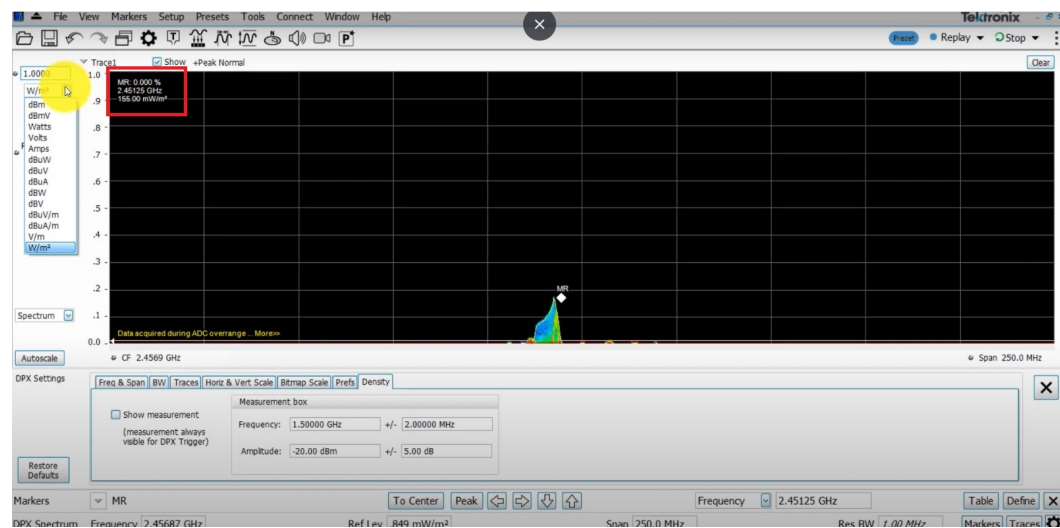


Figure 43. Analysis of transmitter radiation using a spectrum analyzer.

5. Conclusions and Perspectives

This study investigated the possibility of using an RF energy harvesting gadget to wirelessly power an emergency exit sign in case of emergency. An emergency exit sign was equipped with an RF harvester device. During a real experiment, the receiving patch antenna had a reflection coefficient of -22.66 dB and gain of 3.55 dB. This result is acceptable for actual impedance-matching magnitude, close to the predefined value of $50\ \Omega$. For this application, the harvesting antenna meets all specifications. The microwave transmitter station had return loss of -14.86 dB and gain of -10.3 dB. This prototype uses a five-stage voltage multiplier based on the HSMS2820 Schottky semiconductor. It produces a high DC voltage and provides electricity conversion. For each patch antenna surface ($89.36\text{ mm} \times 70.80\text{ mm}$), we achieved 0.483 W at 60 m . Using wireless power technology for emergency exit signs and other emergency systems can be an excellent alternative to direct connections to the primary power grid. Achieving longer distances of wireless power transfer could improve the chances of preventing power outages of emergency lighting, reducing injuries and casualties. The antenna radiation performance using different substrates, such as fabrics and dielectric materials, could be evaluated in future studies. This design could also be extended to include many microstrip patch antennas arranged in specific geometric configurations. As wireless power transfer technology and techniques improve with time, using such emergency exit signs and lighting on a commercial scale will become more feasible.

Supplementary Materials: Video S1: Experimental phase for RF harvester technology (<https://www.youtube.com/watch?v=u96Yyfk3WDY>) (accessed on 21 June 2023), Video S2: Magnetron field strength measurements (<https://www.youtube.com/watch?v=kAN25QFh3Xg&t=68s>) (accessed on 21 June 2023).

Author Contributions: Conceptualization, M.Z.C.; methodology, M.Z.C.; software, M.Z.C. and O.A.; validation, M.Z.C. and G.P.P.; formal analysis, M.Z.C.; investigation, M.Z.C.; resources, M.A. and R.A.-R.; data curation, M.Z.C.; writing—original draft preparation, M.Z.C. and G.P.P.; writing—review and editing, M.Z.C. and G.P.P.; visualization, M.Z.C.; supervision, M.Z.C. All authors have read and agreed to the published version of the manuscript.

Funding: This research received no external funding.

Data Availability Statement: Not applicable.

Conflicts of Interest: The authors declare no conflict of interest.

Abbreviations

WPT	Wireless power transfer
RF	Radio frequency
LED	Light-emitting diode
DC	Direct current
VSWR	Voltage standing wave ratio
CNC	Computer numerical control
Tx	Transmitter
Rx	Receiver
VNA	Vector network analyzer

References

1. NCC. Part E4 Visibility in an Emergency, Exit Signs and Warning Systems (DtS). Available online: <https://ncc.abcb.gov.au/editions/2019-a1/ncc-2019-volume-one-amendment-1/section-e-services-and-equipment/part-e4-dts> (accessed on 14 June 2023).
2. When Are Emergency & Exit Lights Required? Available online: <https://resources.impactfireservices.com/when-are-emergency-exit-lights-required> (accessed on 14 June 2023).
3. Firesafe. Emergency Lighting. Available online: <https://www.firesafe.org.uk/emergency-lighting/> (accessed on 14 June 2023).
4. U.S. Energy Information Administration—EIA. Independent Statistics and Analysis. Available online: <https://www.eia.gov/todayinenergy/detail.php?id=54639> (accessed on 5 June 2023).
5. TEPCO. Top International Level of Quality. Available online: <https://www.tepco.co.jp/en/pg/supply/quality/index-e.html> (accessed on 5 June 2023).
6. EverGlow NA, Inc. Replace Electrical Exit Signs. Available online: <https://www.everglow.us/why-everglow/replace-electrical-exit-signs> (accessed on 14 June 2023).
7. What Is the Purpose of Emergency Lighting? Available online: <https://www.enlighten.com.au/knowledge-centre/what-is-the-purpose-of-emergency-lighting> (accessed on 05 June 2023).
8. Importance of Emergency Lighting Highlighted after Death of Aberdeen Man. Available online: <https://electricalreview.co.uk/2020/08/04/importance-of-emergency-lighting-highlighted-after-death-of-80-year-old-man/> (accessed on 12 December 2022).
9. Emergency Lighting for Schools and Universities. Available online: <https://www.emergencylighting.com/pages/106/> (accessed on 7 June 2023).
10. Institute of Healthcare Engineering and Estate Management. BS 5266-1 Pocket Guide to Emergency Lighting. Available online: https://www.iheem.org.uk/wp-content/uploads/2021/04/Emergency_Lighting_Pocket_Guide_June_2021.pdf (accessed on 5 June 2023).
11. Eaton. How to Meet Regulations for Emergency Lighting. Available online: <https://www.eaton.com/ae/en-gb/markets/buildings/how-we-drive-building-efficiency-and-safety/safe-evacuation/evacuate/basics-emergency-lighting-systems/regulations-for-emergency-lighting.html> (accessed on 5 June 2023).
12. Mohsan, S.A.H.; Islam, A.; Khan, M.A.; Mahmood, A.; Rokia, L.S.; Mazinani, A.; Amjad, H. A Review on Research Challenges, Limitations and Practical Solutions for Underwater Wireless Power Transfer. *Int. J. Adv. Comput. Sci. Appl.* **2018**, *11*, 554–562. [[CrossRef](#)]
13. Patil, P.S.; Padaganur, S. Challenging issues in wire less power transmission methods a survey. *Int. J. Sci. Technol. Res.* **2018**, *7*, 136–139.
14. Ullah, M.A.; Keshavarz, R.; Abolhasan, M.; Lipman, J.; Esselle, K.P.; Shariati, N. A Review on Antenna Technologies for Ambient RF Energy Harvesting and Wireless Power Transfer: Designs, Challenges and Applications. *IEEE Access* **2022**, *10*, 17231–17267. [[CrossRef](#)]
15. Pahlavan, S.; Shooshtari, M.; Jafarabadi Ashtiani, S. Star-Shaped Coils in the Transmitter Array for Receiver Rotation Tolerance in Free-Moving Wireless Power Transfer Applications. *Energies* **2022**, *15*, 8643. [[CrossRef](#)]
16. Beckhusen, R. Army Plan: Wirelessly Recharge Gadgets... From 50 Feet Away. WIRED. Available online: <https://www.wired.com/2012/06/wireless-power/> (accessed on 24 March 2022).
17. Chaari, M.Z.; Al-Rahimi, R. The impact of Wireless Power Charging on the Future of the Battlefield. In Proceedings of the 2021 International Wireless Communications and Mobile Computing (IWCMC), Harbin, China, 28 June–2 July 2021; pp. 1563–1568. [[CrossRef](#)]
18. Akter, N.; Hossain, B.; Kabir, H.; Bhuiyan, A.H.; Yeasmin, M.; Sultana, S. Design and Performance Analysis of 10-Stage Voltage Doublers RF Energy Harvesting Circuit for Wireless Sensor Network. *J. Commun. Eng. Net.* **2014**, *2*, 84–91. [[CrossRef](#)]
19. Chaari, M.Z.; Al-maadeed, S. Wireless Power Transmission for the Internet of Things (IoT). In Proceedings of the 2020 IEEE International Conference on Informatics, IoT, and Enabling Technologies (ICIoT), Doha, Qatar, 2–5 February 2020; pp. 549–554. [[CrossRef](#)]
20. Chaari, M.Z.; Rahimi, R. Light LED directly lit up by the wireless power transfer technology. In Proceedings of the 2017 International Conference on Radar, Antenna, Microwave, Electronics, and Telecommunications (ICRAMET), Jakarta, Indonesia, 23–26 October 2017; pp. 137–141. [[CrossRef](#)]

21. Park, Y.; Youii, D. kW-class Wireless Power Transmission Based on Microwave Beam. In Proceedings of the 2020 IEEE Wireless Power Transfer Conference (WPTC), Seoul, Republic of Korea, 15–19 November 2020; pp. 5–8. [[CrossRef](#)]
22. Liu, J.; Zhao, Z.; Ji, J.; Hu, M. Research and application of wireless sensor network technology in power transmission and distribution system. *Intell. Converg. Net.* **2020**, *1*, 199–220. [[CrossRef](#)]
23. Pinto, D.; Arun, A.; Lenka, S.; Colaco, L.; Khanolkar, S.; Betgeri, S.; Naik, A. Design and Performance Evaluation of a Wi-Fi Energy Harvester for Energizing Low Power Devices. In Proceedings of the 2021 IEEE Region 10 Symposium (TENSYMP), Jeju, Republic of Korea, 23–25 August 2021; pp. 1–8. [[CrossRef](#)]
24. Tran, L.G.; Cha, H.K.; Park, W.T. RF power harvesting: A review on designing methodologies and applications. *Micro Nano Syst. Lett.* **2017**, *5*, 14. [[CrossRef](#)]
25. Sidhu, R.K.; Singh Ubhi, J.; Aggarwal, A. A Survey Study of Different RF Energy Sources for RF Energy Harvesting. In Proceedings of the 2019 International Conference on Automation, Computational and Technology Management (ICACTM), London, UK, 24–26 April 2019; pp. 530–533. [[CrossRef](#)]
26. Kuhn, V.; Lahuec, C.; Seguin, F.; Person, C. A Multi-Band Stacked RF Energy Harvester With RF-to-DC Efficiency Up to 84%. *IEEE Trans. Microw. Theory Tech.* **2015**, *63*, 1768–1778. [[CrossRef](#)]
27. Muncuk, U.; Alemdar, K.; Sarode, J.D.; Chowdury, K.R. Multiband Ambient RF Energy Harvesting Circuit Design for Enabling Batteryless Sensors and IoT. *IEEE Internet Things J.* **2018**, *5*, 2700–2714. [[CrossRef](#)]
28. Huang, Z.; Wang, L.; Zhang, Y.; Liu, R. Design of WPT RF Power Supply Based on Dual Directional Coupler and Capacitor Array Impedance Matching Network. *IEEE Access.* **2020**, *8*, 68209–68218. [[CrossRef](#)]
29. Chen, Y.-S.; Chiu, C.-W. Insertion Loss Characterization of Impedance Matching Networks for Low-Power Rectennas. *IEEE Trans. Compon. Packag. Manuf. Technol.* **2018**, *8*, 1632–1641. [[CrossRef](#)]
30. Silva, E.F.D.; Gomes Neto, A.; Peixeiro, C. Fast and Accurate Rectenna Design Method. *IEEE Antennas Wirel. Propag. Lett.* **2019**, *18*, 886–890. [[CrossRef](#)]
31. Jang, S.-R.; Ryoo, H.-J.; Ahn, S.-H.; Kim, J.; Rim, G.H. Development and Optimization of High-Voltage Power Supply System for Industrial Magnetron. *IEEE Trans. Ind. Electron.* **2012**, *59*(3), 1453–1461. [[CrossRef](#)]
32. He, Y.; Zhao, X.; Zhao, L.; Fan, Z.; Wang, J.K.; Zhang, L.; Ni, C.; Wu, W.J. Design of Broadband Double-Ridge Horn Antenna for Millimeter-Wave Applications. *IEEE Access* **2021**, *9*, 118919–118926. [[CrossRef](#)]
33. Meena, M.S.; Prakash, V. Simulation Results of Rectangular Horn Antenna. *Int. J. Adv. Trends Eng. Technol.* **2018**, *3*, 171–179.
34. Polat, B.; Daşbaşı, R. Analysis of Conical Horn Antenna Radiation over Ground by Directional Currents Method. In Proceedings of the 2021 20th International Conference on Microwave Techniques (COMITE), Brno, Czech Republic, 19–21 April 2021; pp. 1–6. [[CrossRef](#)]
35. Fat, J.; Alam, S.; Surjati, I. Performance analysis at the off body environment in terms of impedance matching, return loss and VSWR for wearable antenna system on different materials. *IOP Conf. Ser. Mater. Sci.* **2019**, *508*, 012075. [[CrossRef](#)]
36. Sharma, R.; Suthar, A.C. Design and Analysis of Pyramidal Horn Antenna as Plane Wave Source for Anechoic Chamber. *J. Adv. Sch. Res. Allied Educ.* **2019**, *16*, 288–295. [[CrossRef](#)]
37. Park, B.; Ryu, H.-G. Link Budget Investigation of Ambient Backscatter Communication. In Proceedings of the 2021 IEEE International Conference on Consumer Electronics-Asia (ICCE-Asia), Gangwon, Republic of Korea, 1–3 November 2021; pp. 1–3. [[CrossRef](#)]
38. Gustafsson, M.; Capek, M. Maximum Gain, Effective Area, and Directivity. *IEEE Trans. Antennas Propag.* **2019**, *67*, 5282–5293. [[CrossRef](#)]
39. Jackson, D.R.; Oliner, A.A. Leaky-Wave Antennas. In *Modern Antenna Handbook*; Balanis, C.A., Ed.; John Wiley & Sons, Inc.: Hoboken, NJ, USA, 2008; pp. 325–367. [[CrossRef](#)]
40. Chaari, M.Z. Wirelessly Powered an Alarm Clock ANENG HTC-1. In Proceedings of the 2022 IEEE International Conference on Consumer Electronics-Asia (ICCE-Asia), Yeosu, Republic of Korea, 26–28 October 2022; pp. 1–5. [[CrossRef](#)]
41. Chaari, M.Z.; Al-Rahimi, R. Energized IoT devices through RF Wireless Power Transfer. In Proceedings of the 2021 International Symposium on Electrical and Electronics Engineering (ISEE), Ho Chi Minh, Vietnam, 15–16 April 2021; pp. 199–203. [[CrossRef](#)]
42. Li, Y.; Hao, Z.-C. A wideband switched beam antenna for full 360 coverage. In Proceedings of the 2017 Sixth Asia-Pacific Conference on Antennas and Propagation (APCAP), Xi'an, China, 16–19 October 2017; pp. 1–3. [[CrossRef](#)]
43. Matsunaga, T.; Nishiyama, E.; Toyoda, I. 5.8-GHz Stacked Differential Rectenna Suitable for Large-Scale Rectenna Arrays With DC Connection. *IEEE Trans. Antennas Propag.* **2015**, *63*, 5944–5949. [[CrossRef](#)]
44. Da Silva, E.F.; Neto, A.G.; Peixeiro, C. Inset Feed Impedance Matching Technique for Rectennas. In Proceedings of the 2022 16th European Conference on Antennas and Propagation (EuCAP), Madrid, Spain, 27 March–1 April 2022; pp. 1–3. [[CrossRef](#)]
45. Ishibashi, K.; Ida, J.; Nguyen, L.-T.; Ishikawa, R.; Satoh, Y.; Luong, D.-M. RF Characteristics of Rectifier Devices for Ambient RF Energy Harvesting. In Proceedings of the 2019 International Symposium on Electronics and Smart Devices (ISESD), Badung, Indonesia, 8–9 October 2019; pp. 1–4. [[CrossRef](#)]
46. Trikolikar, A.; Lahudkar, S. Investigation of Different Optimization Techniques for Rectenna. *Int. J. Recent Innov. Trends Comput. Commun.* **2023**, *11*, 6373. [[CrossRef](#)]
47. Ali, E.M.; Yahaya, N.Z.; Perumal, N.; Zakariya, M.A. Development of Cockcroft Walton Voltage Multiplier for RF Energy Harvesting Applications. *J. Sci. Res. Dev.* **2016**, *47*–51.

48. US EPA. Non-Ionizing Radiation from Wireless Technology. Available online: <https://www.epa.gov/radtown/non-ionizing-radiation-wireless-technology> (accessed on 21 June 2023).
49. FDA. Microwave Ovens. Available online: <https://www.fda.gov/radiation-emitting-products/resources-you-radiation-emitting-products/microwave-ovens> (accessed on 21 June 2023).

Disclaimer/Publisher's Note: The statements, opinions and data contained in all publications are solely those of the individual author(s) and contributor(s) and not of MDPI and/or the editor(s). MDPI and/or the editor(s) disclaim responsibility for any injury to people or property resulting from any ideas, methods, instructions or products referred to in the content.